chemengineering

MDPI

Review

Modifying Superparamagnetic Iron Oxide Nanoparticles as Methylene Blue Adsorbents: A Review

Linh Doan [1,2,3]

[1] Department of Chemical Engineering, International University—Vietnam National University, Ho Chi Minh City 70000, Vietnam; dhlinh@hcmiu.edu.vn
[2] School of Chemical and Environmental Engineering, International University—Vietnam National University, Ho Chi Minh City 70000, Vietnam
[3] Nanomaterials Engineering Research & Development (NERD) Laboratory, International University—Vietnam National University, Ho Chi Minh City 70000, Vietnam

Abstract: Methylene blue (MB) is a hazardous chemical that is widely found in wastewater, and its removal is critical. One of the most common methods to remove MB is adsorption. To enhance the adsorption process, magnetic adsorbents, particularly those based on superparamagnetic iron oxide nanoparticles (SPION), play a vital role. This study focuses on comparing recent novel SPION-based MB adsorbents and how to acquire the critical parameters needed to evaluate the adsorption and desorption mechanisms, including isotherms, kinetics, and thermodynamic properties. Moreover, the review article also discusses the future aspects of these adsorbents.

Keywords: SPION; iron oxide; nanoparticles; methylene blue; adsorption; desorption

Citation: Doan, L. Modifying Superparamagnetic Iron Oxide Nanoparticles as Methylene Blue Adsorbents: A Review. *ChemEngineering* **2023**, *7*, 77. https://doi.org/10.3390/chemengineering7050077

Academic Editor: Alírio E. Rodrigues

Received: 7 August 2023
Revised: 18 August 2023
Accepted: 23 August 2023
Published: 28 August 2023

1. Introduction

The eutrophication of water bodies and a decline in water quality are two environmental problems associated with wastewater discharge. Annually, around 7×10^7 tons of non-biodegradable synthetic dyes are produced worldwide, leading to water pollution [1]. Textile dyes can cause serious problems, such as suppressing plant growth, inhibiting the oxygen supplies for living species, toxicity, mutating species, impairing photosynthesis processes, and carcinogenicity [2,3].

To treat dye effluents, many methods can be considered, including adsorption, flocculation, ion exchange, advanced oxidation processes, chemical precipitation, decantation, biodegradation, and other processes [4]. Among these methods, adsorption is well recognized for being a promising method since, depending on the system, it is efficient, affordable, and easy to handle materials [5]. Conventional treatment methods have been used successfully in a range of wastewater; however, industrial wastewater, which contains significant amounts of toxic compounds such as heavy metals and coloring chemicals, is not well suited for them [6]. Adsorption is one of these methods, and depending on the system, it is well recognized to be a potential method due to its easy handling, low costs, and high efficiency [7].

Furthermore, to enhance wastewater treatment operations, magnetic properties have been researched extensively to modify these systems because they are very effective, utilize minimal energy, and are ecologically beneficial [6]. Nanoparticles with magnetic properties, which have high absorption/adsorption capabilities, charge neutralization, and large surface areas, have been considered effective adsorbents for wastewater treatment. More importantly, when applying the external magnetic field, the adsorbents can be separated rapidly [7–9].

Hence, for researchers who are new (i.e., undergraduate and graduate students) and interested in removing methylene blue from wastewater using the superparamagnetic iron oxide nanoparticles (SPION)-based composite, the aim of this work is to provide a complete overview of:

- How to synthesize SPION-based adsorbents;
- How to characterize the adsorbents;
- How to perform the adsorption and desorption experiments;
- How to calculate the adsorption kinetics, adsorption isotherms, and adsorption thermodynamics properties;
- How to calculate the desorption kinetics;
- Comparing the MB adsorption capacity, kinetics, isotherms, and thermodynamic properties of the most recent adsorbents;
- The future research of methylene blue adsorption by using the SPION-based composite, including recyclability, antimicrobial activities, cost–benefit analysis, and optimization.

1.1. Methylene Blue

As seen in Figure 1, methylene blue (MB) is an aromatic heterocyclic basic dye with the chemical formula $C_{16}H_{18}N_3SCl$. It is also referred to as cationic or primary thiazine dye.

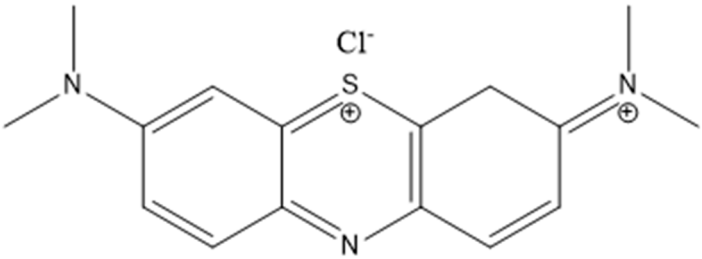

Figure 1. Chemical structure of methylene blue.

The presence of negative polar sites on water molecules causes an attraction for the cationic dye, resulting in the separation of positive ions and the creation of a stable solution with water at room temperature [10]. MB is recognized as a popular cationic dye utilized in a variety of sectors, including the pharmaceutical, food processing, paper, paint, printing, dyeing, and medicine (i.e., diagnostic and therapeutic medicine for both humans and animals) industries [11]. In the textile industry, MB adheres well to the interstitial gaps of cotton fibers and remains stable on fabric. Hence, MB is one of the most used apparel colors.

However, because MB is poisonous, carcinogenic, and non-biodegradable, it may create a variety of environmental hazards in both aquatic and terrestrial life. The danger of MB can also damage human health in a variety of ways, including respiratory discomfort, metal poisoning, stomach pain, blindness, and digestive issues. Furthermore, MB poisoning causes nausea, diarrhea, vomiting, cyanosis, and other symptoms [1].

1.2. Superparamagnetic Iron Oxide Nanoparticles

Depending on the stoichiometry and oxidation state, iron oxide nanoparticles can be in various forms, such as wüstite (FeO), ferrihydrite [$Fe_5HO_8(4H_2O)$], goethite [FeO(OH)], magnetite (Fe_3O_4), maghemite (γ-Fe_2O_3), and hematite (α-Fe_2O_3) [12–14]. Among them, Fe_3O_4 and γ-Fe_2O_3,which have many types of crystalline phases, are the most well-studied materials [15,16]. At room temperature, if these materials have sizes less than 20 nm, the superparamagnetic property (as shown in Figure 2) can occur [16,17]. Superparamagnetic iron oxide nanoparticles (SPION), or Fe_3O_4, are one of the most commonly used materials [16,17].

A single-domain magnetic particle will eventually develop when a ferromagnetic, multidomain sample of Fe_3O_4 is shrunk to a size of less than or equivalent to 15 nm [4,19]. When an external magnetic field is applied inside this particle, the electron exchange coupling inside the domain makes these nanoparticles extremely internally magnetized and becomes superparamagnetic. The particle differs from the ferromagnetic due to the losses of its magnetism after leaving the external magnetic field.

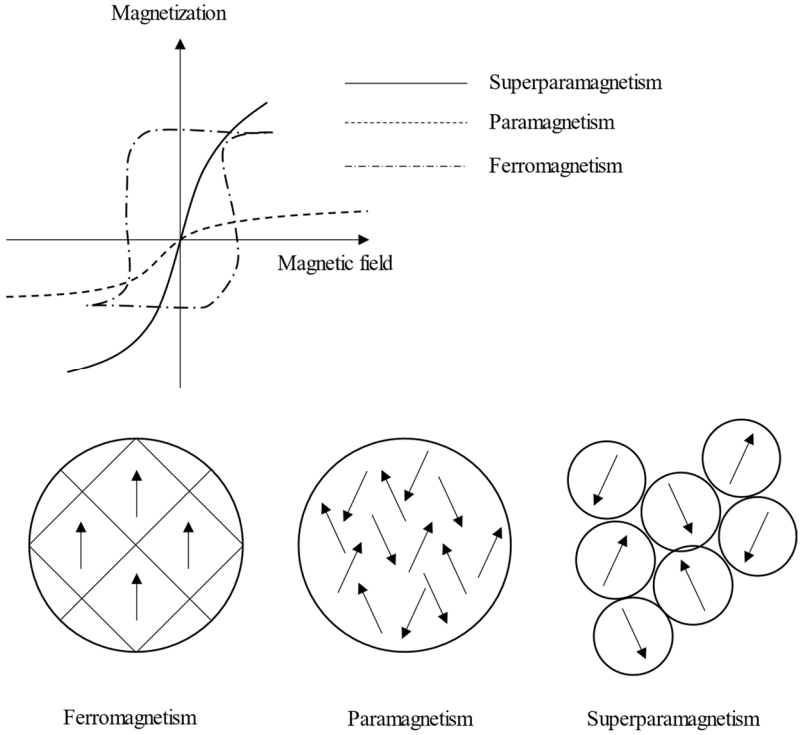

Figure 2. Different types of magnetism [18].

2. SPION Synthesis

The morphology, shape, dispersibility, and size of SPION can be affected by different synthesis methods. Several synthesis routes for magnetic SPION have been reported, including co-precipitation, microemulsion, hydrothermal, electrochemical deposition, aerosol pyrolysis, the sonochemical method, laser pyrolysis, and thermal decomposition [20–33]. Despite various synthesis methods, SPION is usually synthesized via the co-precipitation method, as shown in Figure 3.

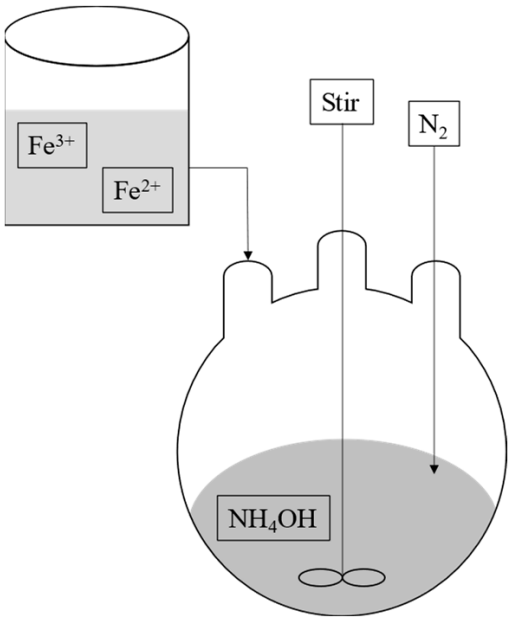

Figure 3. SPION synthesis using the co-precipitation method [34].

When using NaOH as an oxidizing agent, SPION can be formed using the equations below [33,35]:

$$2FeCl_3 + FeCl_2 + 8NaOH \rightarrow Fe_3O_4 + 8NaCl + 4H_2O \quad (1)$$

$$2Fe^{3+} + Fe^{2+} + 8OH^- \rightarrow Fe_3O_4 + 4H_2O \quad (2)$$

$$Fe_3O_4 + 2H^+ \rightarrow \gamma\ Fe_2O_3 + Fe^{2+} + H_2O \quad (3)$$

In this synthesis route, after dissolving iron salts (i.e., $FeCl_3 \cdot 6H_2O$ and $FeCl_2 \cdot 4H_2O$) in diluted HCl [36,37], the mixture is added dropwise to a base under inert atmosphere (Argon or N_2 gas) for 30–60 min to prevent oxidation, which can transform SPION into maghemite (γ-Fe_2O_3) (as shown in Equation (3)) [36,38]. Moreover, by removing the oxygen from the reactor, the SPION size can be reduced from 80 Å to 60 Å [39,40].

However, the co-precipitation method has its own advantages and disadvantages, as shown in Table 1 [41].

Table 1. Advantages and disadvantages of various SPION synthesis methods.

Methods	Advantages	Disadvantages	Factors	Ref
Co-precipitation	Facile Rapid High yield Cheap	Weak size control Aggregation Oxidation	Iron salt precursors (Fe^{3+}:Fe^{2+} = 2:1 mol/mol) Base (ammonia, CH_3NH_2, and NaOH) Optional additional cations (Na^+, K^+, Li^+, NH_4^+, $N(CH_3)_4^+$, $CH_3NH_3^+$) pH = 9–14	[33,34,40,42–45]
Hydrothermal and high-temperature decomposition	Small size distribution High yield Controllable size and shape	High temperature High pressure Long reaction time	Hydrolysis ferrous salts Oxidation of metal hydroxides Pressure > 2000 psi Temperature > 200 °C	[33,43,46–50]
Sol–gel	Controllable kinetics Controllable growth reactions	Expensive Long reaction time	Iron salt precursors Solvents Temperature pH Agitation	[38,51–95]
Aerosol/vapor phase	High yield Non-aggregation	High temperature	Ferric salts Reducing agent	[33]
Electrochemical	Controllable size	Reproducibility	Iron salt precursors	[38,96–98]
Microemulsion	Controllable size Homogeneous	Low yield Long reaction time Substantial number of solvents	Iron salt precursors	

As shown in Table 1, each synthesis method has different advantages and disadvantages. Hence, based on the needed characteristics of SPION, a proper synthesis method should be considered.

3. Modifications of SPION

Bare SPION is hydrophobic, chemically unstable, aggregated, and has low biodegradability. Many researchers have modified the surface of SPION with various inorganic and organic materials, such as silica, polymers, carbon-based materials (i.e., graphite, activated carbon, graphene oxide,. . .), metals, metal oxide nanoparticles, etc., to enhance the performance of these SPION-based MB adsorbents [99–104]. One of these performances can be

reflected in the aggregation of the materials (i.e., SPION [105,106]), stability, adsorption efficiency, adsorption amount, adsorption rate, biocompatibility, and other factors.

One of the most common materials to modify SPION is silica (SPION@SiO_2). Silica creates a shell of negative surface charges, which increases the coulomb repulsion of SPION [37,38,107–113]. SPION@SiO_2 can be synthesized via hydrolysis and condensation of a sol–gel precursor [114], micelles/inverse micelles [115], or the deposition of silica from silicic acid solution [116]. In general, SPION@SiO_2 can be synthesized via four main routes: Stöber, microemulsion, aerosol pyrolysis, and methods based on sodium silicate solution [41]. Similar to bare SPION synthesis, each of these SPION@SiO_2 syntheses also has its own advantages and disadvantages [41].

Similar to silica, to modify the surface of SPION, other inorganic materials can be used. One of the most common inorganic materials used to enhance the adsorption capabilities is carbon. The carbon family includes reduced graphene oxide, graphene oxide, graphite, graphene, graphite oxide, reduced graphite oxide, carbon nanotubes (single-wall, double-wall, and multi-wall), fullerenes, and even activated carbon, as shown in Figure 4.

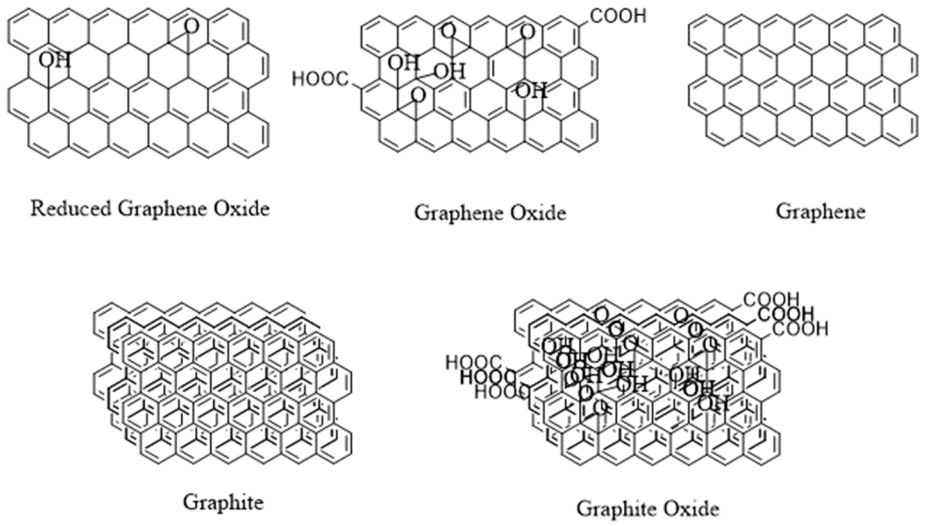

Figure 4. Illustration of molecular structures of different carbon-based materials.

Graphite is the most stable form of carbon, consisting of layers of graphene with covalent and metallic bonds inside each layer and linked to neighboring layers through a delocalized pi-orbital that creates weak van der Waals interactions [117,118]. This unusual shape improves the adsorption by inserting atoms or molecules between the graphite layers [117,118].

On the other hand, activated carbon, one of the most often utilized adsorbents because of its large surface area, strong surface reactivity, high pore value, and appropriate pore distribution as a result of carbonization activation procedures, may be manufactured from a variety of agricultural waste sources [119–121]. Aside from graphite and activated carbon, graphene is a two-dimensional carbon material with a huge surface area and hexagonally organized sp^2-hybridized carbon atoms [122]. As a graphene derivative, graphene oxide (GO) is obtained by oxidizing graphene or graphite by introducing rich-oxygen functional groups [123] on the surface (i.e., the carboxyl group or epoxy) [32,124]. When GO continues to be reduced, reduced graphene oxide (RGO) can be obtained [125]. Graphite oxide, like graphene GO, has a comparable structure to graphite and a high concentration of oxygen-containing functional groups, which can all be synthesized to G, GO, and RGO by utilizing various techniques such as Hummer's method [125,126].

To modify the surface of SPION with carbon-based materials, two main methods can be used: the in situ synthesis [126–132] of SPION and carbon (adjusting the ratio between the carbon and iron precursors [133,134]) or depositing synthesized SPION on to the surface of carbon [125,135].

Other inorganic materials that can be used to modify SPION are metallic elements, which create an inert shell [38] to enhance stability and compatibility [136]. Common metals can be used, such as gadolinium [137–140], titanium dioxide [141], gold [142–144], silver [145,146], etc.

Other types of material that can modify the surface of SPION are organic materials, especially polymers. The two most common methods used are the in situ- and post-annealing coating of polymers on SPION [38]. Common polymers, as shown in Figure 5, can be used in this process, such as polyvinyl alcohol (PVA), chitosan (CS), alginate, polydopamine (PDA), lipids, polyphenol, dextran, poly(N-isopropylacrylamide) (PNIPAM), polyethylene glycol (PEG), starch, polymethylmethacrylate (PMMA), gelatin, poly(ethyleneimine) (PEI), and polyacrylic acid (PAA) [20,38,41,147–159].

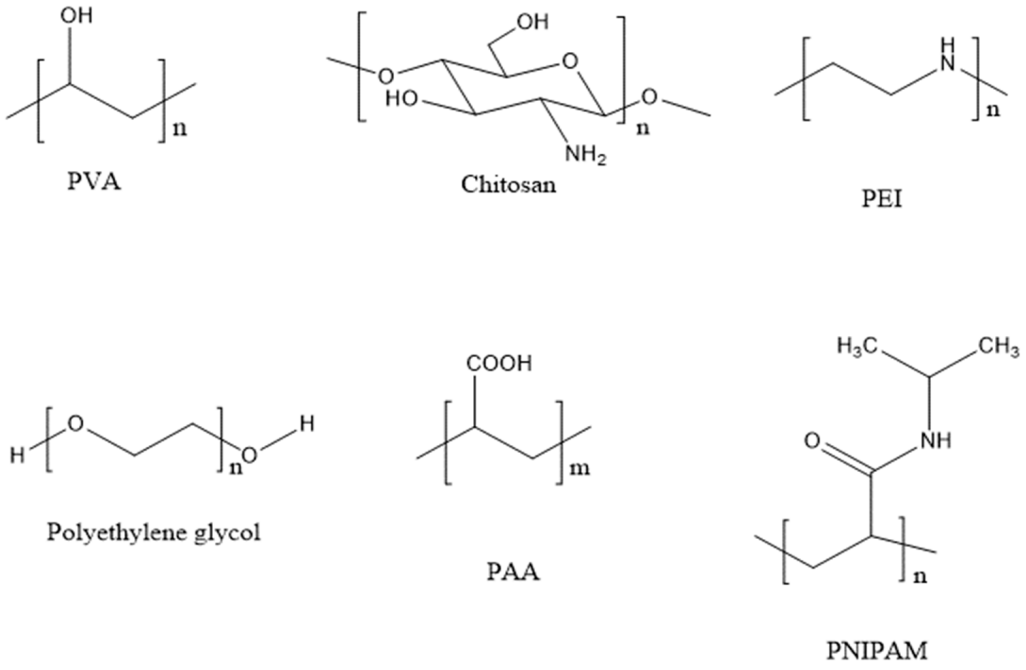

Figure 5. The molecular structures of common polymers modify SPION.

As shown in Figure 5, PVA is one of the vinyl polymer derivatives with solely a C-C bond. The presence of hydroxyl groups in the structure, on the other hand, is the cause of significant water absorption, which is regarded as a drawback when employing PVA as a film or composite. Several methods have been used to minimize the solubility of PVA, such as the inclusion of additives for the usage of films/composite [160]. As a dye removal material, PVA has been widely studied, especially combined with other organic and inorganic materials, such as PVA/GO, PVA/GO/SPION, PVA@walnut shell powder, D-glucose, agar, peroxidase-immobilized Bucky paper/PVA, or PVA/magnesium peroxide [104,161–165]. When PVA creates a shell outside of SPION, the adsorbents can be classified as macromolecules and have a unique polymer gel with great stability and monodisperse efficiency [166–168]. To further enhance the adsorption capabilities, CS can be used in combination with PVA to form hydrogels or enable a film-forming ability [169,170]. If CS is crosslinked to the epoxy groups in GO, a polymer matrix encapsulates GO and modifies the surface of GO as well [28,40–42]. These polymers can coat SPION via encapsulation, as well as graft-to and graft-from methods [20,33]. One of the types of coating is represented graphically in Figure 6 [4].

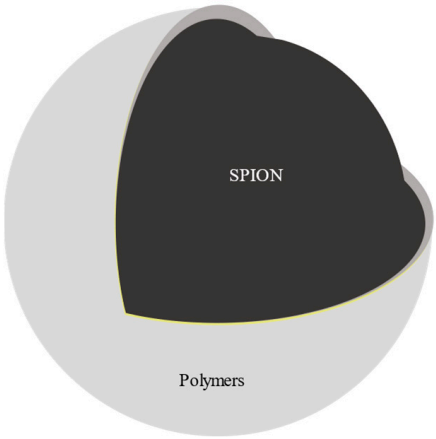

Figure 6. Illustration of polymer-coated SPION.

When coating SPION with CS, PNIPAM, PEI, or PAA, SPION's surface charge can be positive, which increases the dispersibility, stability, and hydrophobicity [171–179]. Moreover, to produce small nanoparticles, using complexing agents such as dextran, starch, PVA, or carboxydextran during the synthesis of SPION can inhibit the nucleation growth process [38,43,180]. Hence, the polymer modification of SPION might decrease aggregation and many other difficulties associated with nanoparticles on the surface while having no influence on the intended qualities of the SPION. Furthermore, the right combination with the polymer may significantly improve the characteristics of SPION. For instance, due to the hydrophilic, water-soluble, biocompatible polymer properties of PEG, the inner SPION-coated polymerized polyethylene glycosylated bilayer has demonstrated outstanding solubility and stability [147,181–183] in an aqueous solution.

4. Characterization

Zeta potential analyzers may be used to evaluate and quantify the adsorbents' surface charge [184]. The structure of magnetite nanoparticles may be established using the X-ray diffractometer (XRD) [185]. The *hkl* planes (220), (311), (422), and (440) of the spinel cubic structure of SPION are represented by the peaks at 30°, 35°, 54°, and 63° in the XRD pattern for SPION [186–189]. However, the XRD analysis can be difficult to distinguish between Fe_3O_4 and maghemite [190]. Hence, the Mössbauer spectra can be used to distinguish them [190].

Other materials bonding to the SPION may also be verified using FTIR techniques (Fourier transform infrared spectroscopy) [32]. The Fe-O-Fe band, which corresponds to the Fe-O bond in bulk magnetite, divides into two peaks in the FTIR spectra of SPION at ~580 and ~450 cm^{-1}, respectively [186,189,191].

UV-VIS spectrophotometry may be used to determine how much MB is loaded onto the particles and how much MB is removed from them [192,193].

By using dynamic light scattering (DLS), the nanoparticles' zeta potential can also be determined [194]. Transmission electron microscopy (TEM) and DLS, respectively, were used to examine the morphology and hydrodynamic diameter of the particles [195]. Additionally, scanning electron microscopy (SEM) may be used to examine the size and shape of the particles, as illustrated in Figure 7 [32].

Overall, the surface morphology can be characterized using SEM and TEM [196]. Various publications [185,197–202] contain TEM and high-resolution TEM pictures of bare SPION and various types of polymer-coated SPION. Atomic force microscopy (AFM) may also be utilized to analyze the morphology in addition to SEM and TEM [203]. A vibrating sample magnetometer (VSM) may be used to test an iron nanoparticle's superparamagnetic [204]. The Brunauer–Emmett–Teller (BET) method may be used to determine the surface area [205,206]. The mesopore pore size distribution, pore volume, pore diameter, and surface area may be determined using Barrett–Joyner–Halenda (BJH) [206,207].

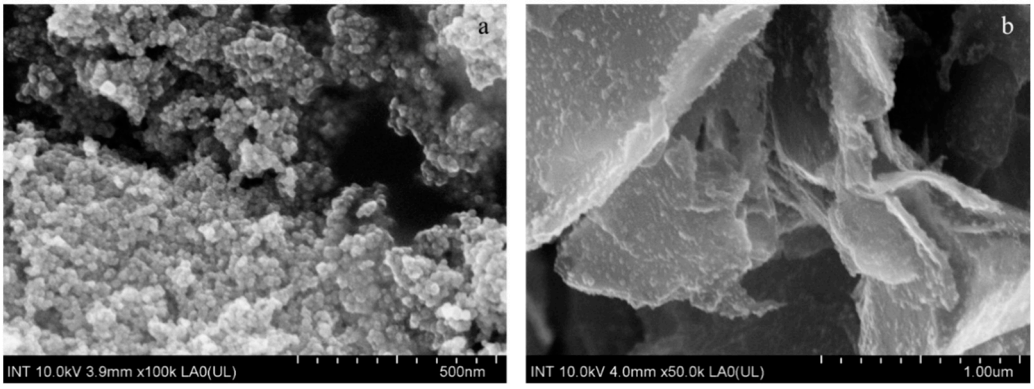

Figure 7. SEM image of (**a**) SPION, (**b**) SPION/PVA/GR.

In BJH analysis, nitrogen gas is usually absorbed into the adsorbents. The volume of adsorbed gas was plotted against the relative pressure p/p_0 to determine the types of adsorptions, as shown in Figure 8.

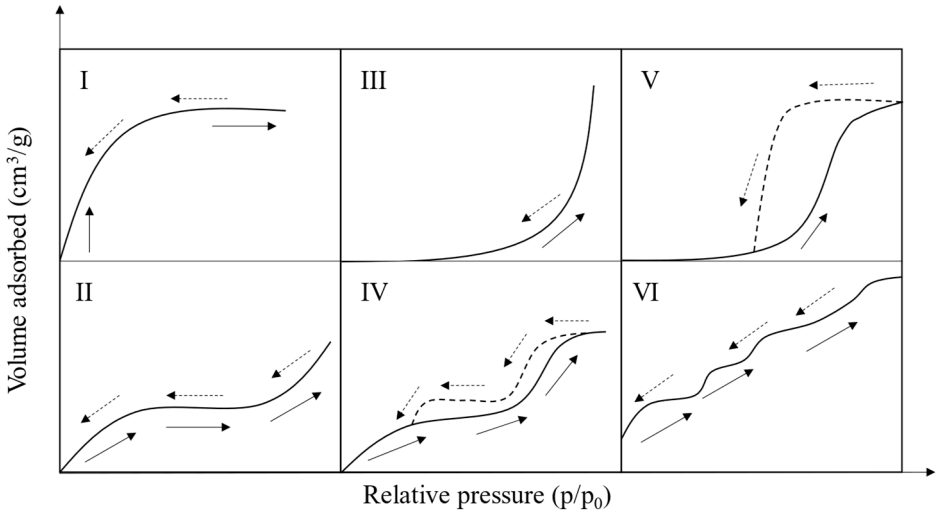

Figure 8. Different types of adsorption isotherms [208,209].

As shown in Figure 8, the type I isotherm indicates that the adsorbents have a microporous (size < 2 nm) structure [209]. When this phenomenon occurs, the amount of adsorption is at its maximum limit [208,209]. This type can be seen with adsorbents made of carbon (i.e., charcoal, activated carbon) [208,209]. The type I isotherm also represents the chemisorption process [210].

The type II isotherm indicates the physical adsorption of gases on non-porous or macroporous (size > 50 nm) adsorbents [209]. The physical adsorption can be monolayer adsorption followed by multilayer adsorption at higher p/p_0 [208,209]. The type II isotherm occurs when gases at temperatures lower than their critical temperature and pressures below but approaching saturation pressure [208,209]. For this type of isotherm, the adsorbent is usually carbons with a combination of micro and mesoporous structures [208,209]. The type II isotherm also represents the physisorption process [210].

The type III isotherm indicates adsorbents with a low adsorption capacity [209]. The type IV isotherm indicates the adsorbents are mesoporous (2 nm < size < 50 nm) [209]. When it comes to type IV isotherms, the largest amount of adsorption occurs before the saturation pressure [208,209]. It shows a hysteresis loop and is linked to the existence of mesoporosity [208,209]. The hysteresis loop is formed by capillary condensation, in which adsorbate molecules condense into tiny capillary gaps [208,209].

At low relative pressures, if the adsorbate interacts weakly with the adsorbent, type V isotherms, which are convex to the relative pressure axis, can be seen [208,209]. Hysteresis is also present in the multimolecular adsorption areas, and it may be observed in both microporous and mesoporous substances [208,209]. In essence, type III's capillary condensation is the basis of this type of isotherm [208,209]. The adsorbed gas quantity is relatively tiny at a low p/p_0, but once a molecule is adsorbed, the force between the gas molecules encourages additional adsorption [208,209]. Types III and V imply the features of a weak gas–solid interaction [208,209]. With a noticeable hysteresis between the adsorption and desorption branches, Type IV is a common isotherm for mesoporous materials, such as the mesoporous carbons produced through template carbonization [208,209].

The type VI isotherm shows that monomolecular layers completely develop before moving onto the following levels [208,209]. It happens on very homogenous, non-porous surfaces when the step height is matched by the monolayer's capacity [208,209].

When determining the type of isotherm model, the geometry change in the hysteresis loop, as shown in Figure 9, during the adsorption and desorption process, is important.

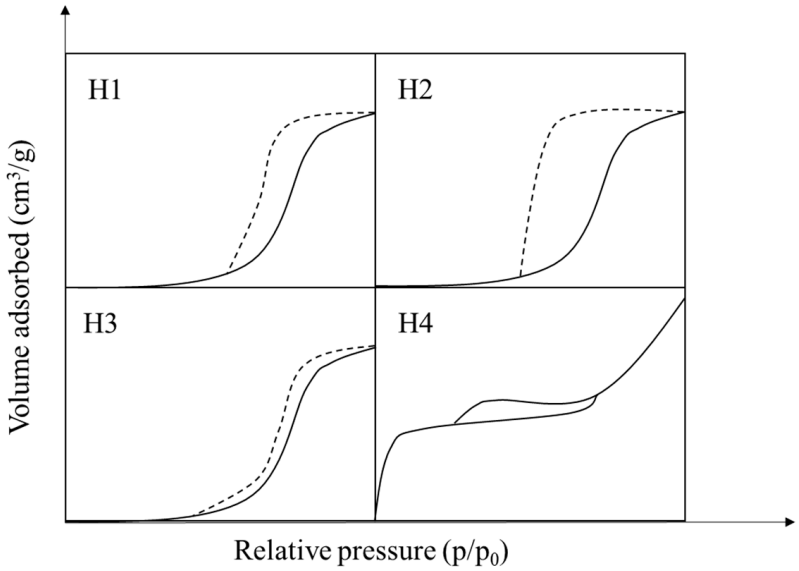

Figure 9. Different types of hysteresis loops [209].

In the cases of H1, H2, H3, and H4, the hysteresis loop represents the channels with uniform sizes/shapes, channels with a pore body greater than pore mouth, adsorbents with wide pore size distributions, and limited amounts of mesopores/micropores, respectively [208,209].

Aside from using FTIR and XRD analyses to determine the structure of the adsorbents, Raman spectroscopy and X-ray photoelectron spectroscopy (XPS) can be used as well, which can detect the molecules' vibrational modes [211,212] and determine the surface chemical composition [196].

5. Adsorption

5.1. Adsorption Methods

First, the calibration curve of MB is necessary. The MB solution, with three known concentrations, is quantified without any adsorbents. Then, with previously known MB concentrations, adsorbents are added to the mixture. The solution is analyzed using UV-VIS at a certain time increment until no change in absorbance is detected. This process was conducted three times. By measuring the concentration of MB in the solution over time, the adsorption kinetics and isotherm model can be determined. The adsorption experiment is repeated at least at two different temperatures to calculate the thermodynamic properties (Gibbs free energy, entropy, and enthalpy) of the adsorption process.

As shown in Table 1b, the MB adsorption (or loading) process can be quantified using multiple equations (Equations (4)–(6)), such as the loading amount ($\mathbf{Q_e}$, mg MB (g nanoparticles)$^{-1}$) [32], dye loading capacity percent (%DL) [32,213], and the entrapment efficiency percent (%EE) [32].

$$\mathbf{Q_e} = \frac{(\mathbf{C_0} - \mathbf{C_e})\mathbf{V}}{\mathbf{m}} \quad (4)$$

$$\%\text{DL} = \frac{\text{Weight of MB absorbed on to the nanoparticles (mg)}}{\text{Weight of nanoparticles (mg)}} \times 100 \quad (5)$$

$$\%\text{EE} = 100 \times \frac{\text{Weight of MB absorbed on to the nanoparticles (mg)}}{\text{Weight of MB initially fed (mg)}} \quad (6)$$

5.2. Adsorption Mechanism

Depending on the adsorbents, many types of adsorption mechanisms can occur. However, MB adsorption may involve bulk diffusion on the surface of the adsorbent, diffusion of MB through the boundary layer of the adsorbent's surface (affected by the rate of adsorption and contact time), adsorption at active sites on the adsorbent's surface, and intraparticle diffusion (i.e., the rate-limiting step) of MB into the pores of the adsorbents [214–217]. Moreover, some other mechanisms can occur, such as ion exchange [218], complexation [218], electrostatic interactions [219], chemisorption [220], physisorption [221], hydrogen bonding [222], π-π* stacking [222], film diffusion [222], van der Waals force [223], hydrophobic interactions [223], ion exchange [224], and hydrogen bonding [224]. These adsorption mechanisms can be determined using an adsorption isotherm, adsorption kinetics, and adsorption thermodynamics models, which can be calculated using the equations below, as shown in Table 2.

Table 2. Equations to calculate kinetic, isotherm, thermodynamic, and other parameters [33].

Models	Equations	Plot	Equation
Kinetics			
Pseudo-first order			
Pseudo-first order [225,226]	Determining the initial steps of the adsorption process. Relationship between changes in concentration and time. The rate depends on the adsorbate concentration [227].		
Nonlinear	$\mathbf{Q_t} = \mathbf{Q_e}(\mathbf{1} - \mathbf{e}^{-\mathbf{kt}})$	$\mathbf{Q_t}$ vs. $\mathbf{t}$	(7)
Linear	$\mathbf{\log}(\mathbf{Q_e} - \mathbf{Q_t}) = \mathbf{\log Q_e} - \left(\frac{\mathbf{k_1}}{\mathbf{2.303}}\right)\mathbf{t}$	$\mathbf{\log}(\mathbf{Q_e} - \mathbf{Q_t})$ vs. $\mathbf{t}$	(7a)
Pseudo-second order			
Pseudo-second order [225,226]	The adsorption rate depends on the adsorption capacity [227]. MB adsorbed on the adsorbents via the chemisorption process (electrons transferring) [170,228–231].		
Nonlinear	$\mathbf{Q_t} = \frac{\mathbf{k_2 Q_e^2 t}}{\mathbf{1} + \mathbf{k_2 Q_e t}}$	$\mathbf{Q_t}$ vs. $\mathbf{t}$	(8)
Linear Type I	$\frac{\mathbf{t}}{\mathbf{Q_t}} = \frac{\mathbf{1}}{\mathbf{k_2 Q_e^2}} + \mathbf{t}/\mathbf{Q_e}$	$\frac{\mathbf{t}}{\mathbf{Q_t}}$ vs. $\mathbf{t}$ $\mathbf{Q_e}$ = 1/slope $\mathbf{k_2}$ = slope^2/intercept $\mathbf{h}$ = 1/intercept	(8a)
Linear Type II	$\frac{\mathbf{1}}{\mathbf{Q_t}} = \left(\frac{\mathbf{1}}{\mathbf{k_2 Q_e^2}}\right)\frac{\mathbf{1}}{\mathbf{t}} + \frac{\mathbf{1}}{\mathbf{Q_e}}$	$\frac{\mathbf{1}}{\mathbf{Q_t}}$ vs. $\frac{\mathbf{1}}{\mathbf{t}}$ $\mathbf{Q_e}$ = 1/slope $\mathbf{k_2}$ = intercept^2/slope $\mathbf{h}$ = 1/slope	(8b)
Linear Type III	$\mathbf{Q_t} = \mathbf{Q_e} - \left(\frac{\mathbf{1}}{\mathbf{k_2 {Q_e}^2}}\right)\frac{\mathbf{Q_t}}{\mathbf{t}}$	$\mathbf{Q_t}$ vs. $\frac{\mathbf{Q_t}}{\mathbf{t}}$ $\mathbf{Q_e}$ = intercept $\mathbf{k_2}$ = −1/intercept × slope $\mathbf{h}$ = −intercept/slope	(8c)
Linear Type IV	$\frac{\mathbf{Q_t}}{\mathbf{t}} = \mathbf{k_2 Q_e^2} - \mathbf{k_2 {Q_e}^2 Q_t}$	$\frac{\mathbf{Q_t}}{\mathbf{t}}$ vs. $\mathbf{Q_t}$ $\mathbf{Q_e}$ = −intercept/slope $\mathbf{k_2}$ = slope^2/intercept $\mathbf{h}$ = intercept	(8d)
	$\mathbf{h_0} = \mathbf{k_2 Q_e^2}$		(9)
Isotherm			

Table 2. *Cont.*

Models	Equations	Plot	Equation
Langmuir [232,233]	$k_a C_e(1-\theta) = k_d \theta$	Assumptions: the adsorption and desorption rates are equal at equilibrium when θ is in direct proportion to the rate of desorption from the surface [233]	(10)
	$\theta = \frac{Q}{Q_m} = \frac{K_L C_e}{(1+K_L C_e)}$		(11)
Nonlinear	$Q_e = \frac{Q^0 K_L C_e}{1+K_L C_e}$	Assumptions: when a single molecule occupies a single surface site, there is no lateral interaction between adjacent adsorbed molecules [233].	(12)
Linear	$\frac{C_e}{Q_e} = \frac{1}{Q^0 K_L} + \frac{1}{Q^0} C_e$	$\frac{1}{Q_e}$ vs. C_e $\frac{1}{Q^0 K_L}$ = slope $\frac{1}{Q^0}$ = intercept $\frac{1}{K_L}$ = slope/intercept	(13)
	$R_L = \frac{1}{1+K_L C_0}$	If $0 < R_L < 1$, then the adsorption was favorable [225,234]	(14)
Freundlich [233]	$1 < n_F < 10$, favorable adsorption [233]. $\frac{1}{n} \approx 0$ and $n_F > 1$, favorable physical process [234,235] $n_F < 1$: bond energies increase with surface density [236].		
Nonlinear	$Q_e = K_F C_e^{1/n_F}$		(15)
Linear	$\log Q_e = \log K_F + \frac{1}{n} \log C_e$		(16)
BET [233]			
Nonlinear	$Q_e = \frac{BCQ^0}{(C_S - C)\left[1+(B-1)\left(\frac{C}{C_S}\right)\right]}$		(17)
Linear	$Q_e = \frac{C}{(C_S - C)Q_e} = \frac{1}{BQ^0} + \frac{(B-1)C}{BQ^0 C_S}$	Q_e vs. $\frac{C}{C_S}$ $\frac{(B-1)}{BQ^0}$ = slope $\frac{1}{BQ^0}$ = intercept B = slope × intercept + 1 $\frac{1}{Q^0}$ = y − intercept[(intercept × slope) + 1]	(18)
Dubinin-Radushkevich (D-R) [233]	E < 0, the sorption process is exothermic [237]. 8 < E < 16 kJ/mol: ion exchange [238–241]. E < 8 kJ/mol: physisorption [238–241]. K_{DR} < 1: surface heterogeneity increases due to the interaction between adsorbents and MB [242].		
	$\ln Q_e = \ln Q_m - K_{DR} \varepsilon^2 =$ $\ln Q_m - K_{DR}\left[RT \ln 1 + \frac{1}{C_e}\right]^2$	$\ln Q_e$ vs. ε^2 K_{DR} = −slope $\ln Q_m$ = intercept average free energy of adsorption, E (kJ mol^{-1}) $E = 2K_{DR}^{-1}$ [233,243]	(19)
Temkin and Pyzhev [244,245]	B_1 decreases when increases in temperature: exothermic [244]		
Nonlinear	$Q_e = \frac{RT}{b} \ln K_{TP} C_e$		(20)
Linear	$Q_e = B_1 \ln K_{TP} + B_1 \ln C_e$	Q_e vs. $\ln C_e$ B_1 = the slope $\ln K_{TP}$ = intercept/slope	(21)
	$B_1 = \frac{RT}{b}$		(22)
Harkins-Jura [244,246]	$\frac{1}{Q_e^2} = \left(\frac{B_2}{A}\right) - \left(\frac{1}{A}\right) \log C_e$	$\frac{1}{Q_e^2}$ vs. $\log C_e$ $\frac{1}{A}$ = −slope B_2 = intercept/slope	(23)
Halsey and Henderson [246,247]	n decreases when increases in temperature: endothermic [246,247]		
Halsey [246]	$\ln Q_e = \left[\left(\frac{1}{n}\right) \ln K_{Ha}\right] - \left(\frac{1}{n}\right) \ln C_e$	$\ln Q_e$ vs. $\ln C_e$ n = −1/slope $\ln K_{Ha}$ = intercept/slope	(24)
Henderson [246]	$\ln[-\ln(1 - C_e)] = \ln K_{He} + n \ln Q_e$	$\ln[-\ln(1 - C_e)]$ vs. $\ln Q_e$ n = slope $\ln K_{He}$ = intercept	(25)
Redlich–Peterson [248]	For simplicity, $K_R = K_L$		
Nonlinear	$Q_e = \frac{K_R C_e}{\left(1+\alpha_R C_e^{\beta_R}\right)}$		(26)
Linear	$\log\left(\frac{K_R C_e}{Q_e} - 1\right) = \beta_R \log C_e + \log \alpha_R$		(27)
Diffusion			

Table 2. *Cont.*

Models	Equations	Plot	Equation
Intraparticle diffusion [225,249]	$\mathbf{Q_t = I + k_i t^{1/2}}$	$\mathbf{Q_t}$ vs. $\mathbf{t^{1/2}}$ $\mathbf{k_i}$ = slope **I** = intercept If **I** = 0: the adsorption process is the intraparticle diffusion. If **I** > 0: the film diffusion and intraparticle diffusion occurred at the same time [250–252] If **I** < 0: combined impacts of surface response control and film diffusion processes [253–255]	(28)
Simplified Elovich model [234,256]	$\mathbf{Q_t = \beta \ln(\alpha\beta) + \beta \ln t}$ **Boundary conditions:** • $\mathbf{\alpha\beta \gg 1}$ • $\mathbf{Q_t = 0}$ at $\mathbf{t = 0}$ • $\mathbf{Q_t = Q_t}$ at $\mathbf{t = t}$	$\mathbf{Q_t}$ vs. ln t $\frac{1}{\beta}$ = slope $\ln(\alpha) = \frac{\text{intercept}}{\text{slope}^2}$	(29)
Boyd's model [234,257]	Plot: Bt vs. t Linear: the controlling step is pore-diffusion [234,258] Nonlinear or linear, not passing through the origin: film diffusion or chemical reaction [234].		
	$\mathbf{f = \frac{Q_e}{Q_t}}$		(30)
	$\mathbf{Bt = -0.4977 - \ln(1 - f)}$	Applied when **f** > 0.85	(31)
	$\mathbf{Bt = \left(\sqrt{\pi} - \sqrt{\pi - \left(\frac{\pi^2 f}{3}\right)}\right)^2}$	Applied when **f** < 0.85	(32)
Thermodynamics [233,234,244]			
	$\mathbf{\ln K_0 = -\frac{\Delta H}{RT} + \frac{\Delta S}{R}}$	$\mathbf{\ln\left(\frac{Q_e}{C_e}\right)}$ vs. $\mathbf{Q_e}$ (Extrapolating it to zero) $\mathbf{K_0 = e^{\ln\left(\frac{Q_e}{C_e}\right)}}$ when $\mathbf{Q_e}$ = 0 $\mathbf{\ln K_0}$ vs. 1/T $\mathbf{-\frac{\Delta H}{R}}$ = slope $\mathbf{\frac{\Delta S}{R}}$ = intercept	(33)
	$\mathbf{\Delta G = \Delta H - T\Delta S}$	$\mathbf{\Delta G > 0}$: not spontaneous [234]. $\mathbf{\Delta G > 0}$: spontaneous. $\mathbf{\Delta S < 0}$: the randomness decreasing on the surface. $\mathbf{\Delta S > 0}$: the randomness increasing on the surface [234]. $\mathbf{\Delta H < 0}$: exothermic $\mathbf{\Delta H > 0}$: endothermic [234], monolayer adsorption [259]. Small $\mathbf{\Delta H > 0}$: weak forces of attraction, weak electrostatic interactions, and the existence of loose bonding between adsorbents and MB [260–262]. $\mathbf{\Delta H < 40 \frac{kJ}{mol}}$: dominated by physisorption [221,263] $\mathbf{\Delta H < 20 \frac{kJ}{mol}}$: dominated by van der Waals forces [264].	(34)
Activation energy			
Arrhenius [221,265,266]	$\mathbf{\ln K_{ads} = \ln A - \frac{E_A}{RT}}$	$\mathbf{\ln K_{ads}}$ vs. $\mathbf{1/T}$ (K^{-1}) $\mathbf{-E_A/R}$ = slope $\mathbf{E_A}$ < 40 kJ/mol: chemisorption [267] 25 < $\mathbf{E_A}$ < 30 kJ/mol: diffusion-controlled [268] $\mathbf{E_A}$ > 40kJ/mol: physisorption [265,266].	(35)
Fittings parameters			
Chi-square	$\mathbf{\chi^2 = \sum_{i=1}^{m} \frac{(Q_{e,exp} - Q_{e,calc})^2}{Q_{e,exp}}}$	Small $\mathbf{\chi^2}$: calculated values are similar to experimental data [244]. Large $\mathbf{\chi^2}$: calculated values are different from experimental data [244]	(36)

Moreover, the physical and chemical characteristics of the adsorbents, the concentration of the adsorbate, the temperature, pressure, shaking time, stirring speed, contact time, ionic strength, pH value, and the presence of an interfering material all affect the adsorption capacity and rate [233,269–274]. For instance, by increasing the ionic strength, the MB adsorption capacity in aqueous GO and amberlite can increase and decrease, respectively [269,274]. Hence, several studies should be carried out to determine which adsorption condition yields the most efficient adsorption capacity and adsorption rate. However, the effects on MB adsorption by varying the adsorption temperature, pH, and initial MB concentration can be predicted.

5.3. Effects on Temperature

Temperature is one of the variables that can affect the adsorbed amount of MB on the adsorbents. Based on the change in temperature and the adsorbed amount, adsorption thermodynamics parameters can be calculated. Based on these parameters, if the adsorption is endothermic, the adsorption capacity increases with the increases in temperature [275–277]. On the other hand, if the adsorption capacity decreases with the increases in temperature, the adsorption process is exothermic [275–277]. The endothermic or exothermic processes can be validated via the positive or negative values of enthalpy (ΔH), respectively.

5.4. Effects on pH

Depending on the surface charge of the adsorbents at different pHs, the adsorption capacities can vary. However, the optimal pH range for methylene blue (MB) adsorption is between 6 and 8. When the functional group in the adsorbent has the highest ability to bind the dye, pH 7 to 8 may be the range where MB reaches its isoelectronic point [278,279]. When the adsorbent has a positive charge, at basic conditions, the adsorbent's capacity to bind MB is reduced because the dye and free OH^- ions compete for the surface area Hence, at a higher pH, if the adsorbent has a negative charge, the adsorption capacity will increase greatly [219]. If the surface charge density of the adsorbent is smaller than the pH, the binding of positively charged MB can be enhanced [222]. Hence, if the adsorbent has a charge density smaller than the pH, at lower pHs, the H^+ in a solution creates a repulsive force between the positive charges and inhibits the adsorption process [280].

5.5. Effects on Initial Concentration

With an increase in the initial concentration of MB, leading to a larger driving force overcoming the resistance to the mass transfer, the adsorbed percentage exponentially decreased while the quantity absorbed increased exponentially [281]. This suggests that the high initial concentration of MB requires more active sites [214,282]. The increase in the initial concentration of MB also increases the interaction between MB and the adsorbents, leading to an increase in the adsorbed amount. As the initial concentration of MB increases, the adsorption rate, in the beginning, increases as well due to the bulk diffusion—a large amount of available active sites on the surface of the adsorbents. This phenomenon also indicates that, with an increase in the adsorbent mass, the number of adsorption sites also increases, leading to an increase in MB's adsorption amount [192,281]. Due to the change in the adsorbed amount and the adsorption rate, the time needed to reach equilibrium also varies. Basically, regarding the increases in initial MB concentration, the time to reach equilibrium is longer due to the lack of adsorption sites on the adsorbent's surface, leading to the intraparticle diffusion process (i.e., the rate-limiting step)—unbound MB molecules must penetrate the boundary layer of the adsorbent's surface and enter into the adsorbent's particles [192,193,283,284].

5.6. Adsorption Comparison Studies

Table 3 lists the comparison of diverse types of SPION-based MB adsorbents.

Table 3. Comparison of the maximum adsorption capacity of SPION-based MB adsorbents.

Adsorbent	Adsorption Capacity (mg/g)	Isotherm, Kinetics, Thermodynamics	Ref.
SPION	45.43	Langmuir, PSO	[285]
SPION (*Zanthoxylum armatum* DC. via green route method)	7.26	Langmuir, PSO	[286]
SPION (*P. factra* extract via green route method)	26.81	Freundlich, PSO	[287]
SPION@C using $FeSO_4$, FeS_2, PVP K30 as raw materials	17.26	Redlich–Peterson, PSO	[288]

Table 3. *Cont.*

Adsorbent	Adsorption Capacity (mg/g)	Isotherm, Kinetics, Thermodynamics	Ref.
SPION@C using $FeCl_3 \cdot 6H_2O$, citrus pectin as raw materials	141.3	Freundlich, PSO	[289]
SPION@C using citrus bergamia as raw materials	31	PSO, intraparticle diffusion, spontaneous, endothermic	[290]
SPION@Carbon sheets	95	Freundlich, PSO	[291]
SPION@Graphene	45.27	Langmuir, PSO	[292]
SPION@NH_2-MWCTNs	178.5	Langmuir, PSO, spontaneous, exothermic	[293]
SPION/EG	76.2	Redlich–Peterson, PSO	[294]
SPION/GO	280.26	Langmuir, PFO, spontaneous, endothermic	[295]
SPION/MWCNT	48.06	Langmuir, PSO, film diffusion, intraparticle diffusion	[225]
SPION/moringa seed shell biochar	219.60	Freundlich, PSO, Elovich, spontaneous, endothermic, chemisorption	[296]
SPION/pyrolyzed sorghum straw	136.53	Langmuir, PSO, intraparticle diffusion	[297]
SPION/CS/p(Aam/NVIm) hydrogels	860	Langmuir, PSO	[298]
PVA/SA/SPION@KHA gel beads	781.92	Langmuir, PSO, spontaneous, endothermic	[299]
SPION-MWCNT-Bentonite	48.2	Redlich–Peterson, PFO, physisorption, non-spontaneous, endothermic	[300]
SPION/AMMT	106.38	Langmuir, PSO	[301]
SPION/Bentonite/Sawdust	144.2	Freundlich, PSO	[302]
SPION/TiO_2-graphene sponge	224	Temkin, PSO, spontaneous, endothermic	[303]
Alg/Clin/SPION	12.48	Langmuir, PSO, spontaneous, exothermic	[280]
Clin/SPION	45.66	Langmuir, PSO, spontaneous, exothermic	[280]
Alg beads impregnated with SPION/CS@Zeolite	6.14	Freundlich, PSO, spontaneous, exothermic	[304]
H_2SO_4 crosslinked SPION/CS	20.408	Langmuir	[305]
SPION@SiO_2@HKUST-1	434.78	Langmuir, PSO	[306]
SPION@SiO_2@Zn–TDPAT	20.83	Langmuir, PSO, spontaneous, endothermic	[307]
SPION@MIL-100(Fe)	221	Langmuir, PSO, spontaneous, exothermic	[308,309]
SPION-COOH/HKUST-1	118.6	Langmuir, PSO, spontaneous, endothermic	[310]
SPION/PVP embedded HKUST-1	2.96	Langmuir, PSO, spontaneous, endothermic	[311]
SPION/HKUST-1/GO	150	Langmuir, PFO	[312]
SPION@PAA/MIL-100(Fe)	34.53	Langmuir, PSO, spontaneous, endothermic	[313]
SPION/g-C_3N_4	20.5	PSO	[314]
Co doped Fe-BDC MOF	23.92	Langmuir, PSO, spontaneous, endothermic	[315]
SPION/PPy/C	90.9	Langmuir, PSO	[316]
CA/CS/SWCNT/SPION/TiO_2	14.3	Redlich–Peterson, PSO	[317]
SPION@PDA/CMC	217.43	Langmuir, PSO, spontaneous, endothermic	[318]
SPION-GLP@CAB	70.43	Langmuir, PFO, spontaneous, exothermic	[319]
SDS@SPION	62.43	Langmuir, PSO, spontaneous, endothermic	[320]
SPION@PPy/RGO	270.3	Langmuir, PSO, spontaneous, endothermic	[321]
SPION/Ni/C	175.2		[322]
SPION/GNS	35.42	Langmuir, PSO, spontaneous, endothermic	[323]
Ti_3C_2@SPION	11.68	Langmuir, non-spontaneous, exothermic	[324]
BC-GO@SPION	9.87	Freundlich, PSO, spontaneous, endothermic	[325]
Cellulose/SPION	19.49	Dubini-Radushkevich	[326]

Table 3. *Cont.*

Adsorbent	Adsorption Capacity (mg/g)	Isotherm, Kinetics, Thermodynamics	Ref.
GO/SPION/CS	30.01	Langmuir	[327]
Rectorite/SPION/ZnO	35.1	Langmuir	[328]
SPION@C/Ag	40.16	Langmuir, PSO, spontaneous, endothermic	[329]
Boehmite@SPION@PLA@SiO_2	70.03	Langmuir, PSO	[330]
RGO-Fe_2O_3-SPION	72.8	Langmuir, PSO	[331]
SPION@SiO_2–VTEOS–DMDAAC	109.89	Freundlich, PSO	[332]
Lignin/SPION	203.66	Langmuir	[333]
Fe_3C/SPION/C nanosheets	918	Langmuir, PSO, Elovich, spontaneous, endothermic	[334]
paAm/CS/SPION	1603	Langmuir, PFO	[335]
SPION@SiO_2	123	Freundlich, PFO	[336]
Multi-carboxyl functionalized SPION@SiO_2	34.75	Langmuir, PSO	[337]
SPION@SiO_2-APTA	46.24	Freundlich, PSO	[338]
SPION@SiO_2-EDA-COOH	43.15	Freundlich, PSO	[339]
Mesoporous SPION@SiO_2	33.12		[340]
SPION@ZIF-8	20.2		[341]
HPPs-$BiVO_4$/SPION	33.6		[342]
P(MMA-AA-DVB)/$BiVO_4$/ SPION microcapsules	5		[343]
m-SPION0.3-C/D0.5 hydrogel	529		[344]

where CS: Chitosan; SPION: Superparamagnetic iron oxide nanoparticles; MWCNT: Multi-wall carbon nanotubes; SA: Sodium alginate; KHA: Potassium humate; PVP K30: Polyvinylpyrrolidone K30; $FeSO_4$: Iron (II) sulfate; FeS_2: Iron disulfide; $FeCl_3 \cdot 6H_2O$: Ferric (III) chloride hexahydrate; SiO_2: Silicon dioxide; pAam: Polyacrylamide; pVNIm: Poly N-vinyl imidazole; EG: Expanded graphite; GO: Graphene oxide; TiO_2: Titanium dioxide; PVA: Polyvinyl alcohol; AMMT: Activated montmorillonite; H_2SO_4: Sulfuric acid; HKUST-1: MOF-199; Co: Cobalt; Fe: Iron; BDC: Benzene dicarboxylic acid or terephthalic acid; MOF: Metal-organic framework; Zn: Zinc; TDPAT: 2,4,6-tris (3,5-dicarboxyl phenylamino)-1,3,5-triazine; MIL-100: Materials of Institute Lavoisier-100 (MOF); PAA: Polyacrylic acid; ZIF-8: Zeolite imidazolate frameworks; HPPs: Hybrid porous particles; BiVO4: Bismuth vanadate; P(MMA-AA-DVB): poly(methyl methacrylate-methyl acrylate-divinylbenzene) (P(MMA-MA-DVB)); m-SPION0.3-C/D0.5 hydrogel: SPION modified with citrate ions entrapped in aluminum-carboxymethyl cellulose/dextran sulfate beads; PPy: Polypyrrole; CA: Cellulose acetate; SWCNT: Single-walled carbon nanotube; PDA: Polydopamine; CMC: Carboxymethyl chitosan; GLP: Guava leaves powder; SDS: Sodium dodecyl sulfate; RGO: Reduced graphene oxide; APTA: 5-aminoisophthalic acid; EDA-COOH: Carboxylated ethylenediamine; GNS: Graphene nanosheet; BC: Black cumin seeds; PLA: Polylactic acid; VTEO: Triethoxyvinylsilane; DMDAAC: Dimethyl diallyl ammonium chloride; PSO: Pseudo-second order; PFO: Pseudo-first order; Alg: Alginate; Clin: Clinoptilolite.

As shown in Table 3, the adsorption capacities and adsorption mechanisms can be affected by various conditions, such as the synthesis route of bare SPION, the materials that were used to modify the surface of SPION, and the adsorption conditions (pH, MB initial concentration, adsorbents dosage, temperature).

6. Desorption

6.1. Desorption Methods [4]

After the adsorption experiment, the MB- loaded adsorbents were removed from the aliquot using neodymium magnets. Then, the MB-loaded adsorbent container was filled with deionized water, which has a certain pH. Each day, UV-Vis spectrometry was used to quantify the concentration of MB. The aliquot was placed back into the container after being analyzed by the UV-Vis spectrometry. Every certain day, the aliquot in falcons was changed back to MB-free DI again. The desorption process duration can vary depending on the equilibrium point. This process was conducted three times.

6.2. Desorption Mechanism

Moreover, various types of mathematical models, such as the Higuchi, zeroth order, and Korsmeyer–Peppas models, can be used to determine the desorption kinetics [345,346]. These models each have their own disadvantages and advantages. The desorption kinetics study was calculated using the equations shown in Table 4 [345,346]:

Since the equation only contains the rate constant ($k_0 k_o$) and the released mass fraction at time t (M_t), the zeroth order model shows that the release rate of MB does not rely on the concentration of MB.

Table 4. Desorption kinetics equations.

Model	Linear	Nonlinear
Zeroth order	$\mathbf{M_t = k_0 t}$	$\mathbf{M_t = k_0 t}$
Higuchi	$\mathbf{\log(M_t) = \log(k_H) + 0.5\log(t)}$	$\mathbf{M_t = k_H t^{1/2}}$
Korsmeyer–Peppas	$\mathbf{\log\left(\frac{M_t}{M_\infty}\right) = \log(k_{KP}) + n_{KP}\log(t)}$	$\mathbf{\frac{M_t}{M_\infty} = (k_{KP})(t^{n_{KP}})}$

The release of the MB from the insoluble matrices (planar system) is described by the Higuchi model. This model works best when non-swelling polymers are used in conjunction with water. This model assumes that the diffusion happens only in one dimension, MB particles are much smaller than the system thickness, and the MB diffusivity is constant.

Developed from the Higuchi model, the Korsmeyer–Peppas model or the "Power law" describes the release of the adsorbate from polymetric matrices. When the release mechanism is unknown, or there are many release phenomena present, the Korsmeyer–Peppas model makes it easier to examine the release of MB [347]. If the adsorbent has a cylindrical shape, the n values can tell the types of desorption as follows, shown in Table 5 [348,349]:

Table 5. Explanation of n_{KP} values.

n_{KP} Values	Types of Desorption
$0.45 \leq n_{KP}$	Fickian diffusion
$0.45 < n_{KP} < 0.89$	Non-Fickian diffusion (combination of diffusion and matrix-degradation mechanisms) [350,351]
$n_{KP} = 0.89$	Case II (relaxational) transport
$n_{KP} > 0.89$	Super case II

7. Future Research

7.1. Recyclability

Recyclability is a crucial component of any adsorbent material, including SPION-based MBs, because it directly affects the adsorption process's economic and environmental sustainability. Researchers can evaluate the number of times MB adsorbents may be reused before their adsorption capability dramatically reduces by analyzing their recyclability. Many research publications, however, do not provide experimental data or calculations about the recycling and reuse of SPION-based MBs.

Several factors contribute to the relevance of recyclability. For starters, it affects the adsorption process's cost-effectiveness. If MB adsorbents can be recycled several times, the requirement for regular replacement is reduced, cutting the total cost of the adsorption process. Furthermore, recyclability minimizes the need for fresh MBs, which can be costly to synthesize or obtain, making the process more economically viable. Furthermore, recyclability is critical in decreasing the environmental effect of SPION-based MB adsorbents. SPION manufacturing requires energy-intensive procedures and may need the use of hazardous chemicals. By increasing MB recyclability, the overall consumption of SPIONs

may be reduced, resulting in a reduction in the environmental footprint associated with their synthesis and disposal. Understanding the constraints and degradation mechanisms connected with the recycling process allows scientists to work on enhancing a material's qualities and coating methods to improve the adsorbent's lifetime and recyclability.

7.2. Antibacterial Properties

The capacity of SPION-based MB adsorbents to display antimicrobial qualities, such as limiting the development or killing of microbes, is referred to as antimicrobial activity. While the major emphasis of these adsorbents is frequently placed on their adsorption capacities, their potential antimicrobial activities can play a significant role in a variety of applications, notably in water treatment and environmental remediation. Several reasons contribute to the relevance of antibacterial activity in SPION-based MB adsorbents. For starters, the presence of harmful microorganisms in water treatment applications might represent serious health dangers. Several bacteria may cause serious health problems in wastewater, such as *Salmonella* spp., *Shigella* spp., *Escheria* spp., *Yersinia* spp., *Leptospira* spp., *Aeromonas hydrophila*, *Legionella pneumophila*, *Vibrio cholerae*, *Pseudomonas*, *Mycobacterium* spp., and *Klebsiella* spp. [352]. It is feasible to minimize the microbial load and limit disease transmission through treated water by integrating antimicrobial characteristics into MB adsorbents. Regardless of these potential dangers, many published research studies fail to analyze or address the antibacterial properties of SPION-based MB adsorbents. This omission inhibits our comprehension of their larger uses and prevents us from exploring their full potential. To investigate the antibacterial activities of SPION-based MB adsorbents, many different techniques can be used, such as the agar disk-diffusion method, antimicrobial gradient method, agar well-diffusion method, agar plug-diffusion method, cross-streak method, dilution method, broth dilution method, and agar dilution method [353].

7.3. Optimization

The size, shape, and geometry of SPIONs can affect the magnetic field, leading to the retrieval of SPION-based MB adsorbents. Moreover, when modifying SPIONs, the zeta potential values, stability, and surface charges of the adsorbents can be changed as well, affecting the MB adsorption capacities, depending on the acidic or basic environment. By balancing these factors, economical and effective SPION-based MB adsorbents can be designed. Moreover, the cost analysis of these adsorbents should be investigated further. Additionally, determining the relationship between the size, shape, and geometry of the adsorbent and the MB adsorption capacities can be investigated further. In addition, when the antibacterial properties of SPION-based MB adsorbents are determined by incorporating this factor, these adsorbents can have dual functionalities—adsorbing MB and inhibiting the growth of bacteria, leading to a real-world application of these adsorbents. Hence, when taking account of these factors, optimization studies can be the direction of future research.

8. Conclusions

The SPION-based MB adsorbents play a crucial role in removing MB from wastewater. With the superparamagnetic property, the adsorbents can be extracted easily via an external magnetic field. SPIONs can be synthesized via different techniques; among them, the most facile method is co-precipitation. By modifying the surface of SPIONs, these adsorbents can have different adsorption mechanisms. Hence, evaluating the isotherm models, kinetics models, and thermodynamic models is important. Moreover, the desorption process is also important to research, and the review article shows several types of methods to evaluate the desorption mechanisms. However, recently, the recyclability of SPION-based MB adsorbents is still not one of the main concerns for most of the research articles. Additionally, the antimicrobial activities of these adsorbents are almost completely neglected, which contributes to the limitations of the applications of these SPION-based MB adsorbents.

Funding: This research received no external funding.

Data Availability Statement: All data that support the findings of this study are included within the article.

Acknowledgments: The author acknowledges Tran P.T. Quach, Khanh G. Huynh, Tu M.D. Nguyen, Lam V.H. Tang, and Tan M. Le from the International University—Vietnam National University, Ho Chi Minh City, Vietnam.

Conflicts of Interest: The author declares no conflict of interest.

Abbreviations

$\mathbf{C_0}$	Initial concentration (mg/mL)	$\mathbf{K_F}$	Constant of the relative adsorption capacity of the adsorbent
$\mathbf{C}_t$	Concentration at time t (mg/mL)	$\mathbf{Q_{mDR}}$	Theoretical saturation capacity
$\mathbf{V}$	Reaction volume (mL)	$\mathbf{K_{DR}}$	The activity coefficient related to the mean free energy of adsorption
$\mathbf{m}$	Nanoparticles mass (g)	ε	The Polanyi potential
$\mathbf{Q_e}$	The amounts of adsorbate (MB) adsorbed at the equilibrium (mg/g)	$\mathbf{R}$	Universal gas constant
$\mathbf{Q_t}$	MB mass adsorbed at time t (mg/g)	$\mathbf{T}$	Temperature
$\mathbf{C_e}$	The equilibrium aqueous-phase concentration adsorbate (mg/L)	$\mathbf{K_{TP}}$	Equilibrium binding constant
$\mathbf{Q}^0$	The theoretical adsorption capacity or the monolayer adsorption capacity (mg/g)	$\mathbf{B_1}$	Related to the heat of adsorption
$\mathbf{K_L}$	Constant related to the free adsorption energy and the reciprocal of the concentration at which half saturation of the adsorbent is reached	$\mathbf{K_{Ha}}$	The Halsey isotherm constant
$\mathbf{Q_m}$	The quantity of adsorbate adsorbed in a single monolayer	$\mathbf{k_i}$	Intraparticle diffusion rate constant
θ	The fractional surface coverage	$\mathbf{I}$	Constant
$\mathbf{k_a}$	The respective rate constant for adsorption	α	The theoretical initial adsorption rate
$\mathbf{k_d}$	The respective rate constant for desorption	β	The theoretical desorption constant
$\frac{1}{\mathbf{n_F}}$	The intensity of the adsorption	$\Delta\mathbf{G}$	Gibbs free energy change
$\Delta\mathbf{S}$	Entropy change	$\Delta\mathbf{H}$	Standard enthalpy change
$\mathbf{K_0}$	Thermodynamic equilibrium constant in the adsorption process	$\mathbf{M_t}$	Released mass fraction at a time (t)
$\frac{\mathbf{M_t}}{\mathbf{M_\infty}}$	Released fraction mass	$\mathbf{K_H}$	Higuchi release rate constant
$\mathbf{K_{KP}}$	Korsmeyer–Peppas release rate constant	$\mathbf{n_{KP}}$	Korsmeyer–Peppas release exponent factor
$\mathbf{k_o}$	Constant mass fraction at a time (t) release	$\mathbf{k}_1$	Pseudo-first-order rate constant (s^{-1})
χ^2	Chi-square value	$\mathbf{k}_2$	Pseudo-second-order rate constant (s^{-1})
$\mathbf{M}_\infty$	The amount of MB at equilibrium state	$\mathbf{K_R}$	Modified Langmuir constant (dm^3/g)
$\alpha_\mathbf{R}$	Redlich–Peterson constant (dm^3/g)	β_R	Redlich–Peterson constant (dm^3/g)
$\mathbf{h_0}$	The initial adsorption rate (mg g^{-1} min^{-1})	$\mathbf{E_A}$	Arrhenius activation energy (kJ/mol)
$\mathbf{R}$	Universal gas constant (8.314 J mol^{-1} K^{-1})		

References

1. Al-Tohamy, R.; Ali, S.S.; Li, F.; Okasha, K.M.; Mahmoud, Y.A.-G.; Elsamahy, T.; Jiao, H.; Fu, Y.; Sun, J. A Critical Review on the Treatment of Dye-Containing Wastewater: Ecotoxicological and Health Concerns of Textile Dyes and Possible Remediation Approaches for Environmental Safety. *Ecotoxicol. Environ. Saf.* **2022**, *231*, 113160. [CrossRef] [PubMed]
2. Ali, H. Biodegradation of Synthetic Dyes—A Review. *Water Air Soil Pollut.* **2010**, *213*, 251–273. [CrossRef]
3. Lellis, B.; Fávaro-Polonio, C.Z.; Pamphile, J.A.; Polonio, J.C. Effects of Textile Dyes on Health and the Environment and Bioremediation Potential of Living Organisms. *Biotechnol. Res. Innov.* **2019**, *3*, 275–290. [CrossRef]
4. Quach, T.P.T.; Doan, L. Surface Modifications of Superparamagnetic Iron Oxide Nanoparticles with Polyvinyl Alcohol, Chitosan, and Graphene Oxide as Methylene Blue Adsorbents. *Coatings* **2023**, *13*, 1333. [CrossRef]
5. Damasceno, B.S.; da Silva, A.F.V.; de Araújo, A.C.V. Dye Adsorption onto Magnetic and Superparamagnetic Fe_3O_4 Nanoparticles: A Detailed Comparative Study. *J. Environ. Chem. Eng.* **2020**, *8*, 103994. [CrossRef]
6. Wang, Y.; Gu, X.; Quan, J.; Xing, G.; Yang, L.; Zhao, C.; Wu, P.; Zhao, F.; Hu, B.; Hu, Y. Application of Magnetic Fields to Wastewater Treatment and Its Mechanisms: A Review. *Sci. Total Environ.* **2021**, *773*, 145476. [CrossRef]
7. Dada, A.O.; Olalekan, A.P.; Olatunya, A.M.; Dada, O. Isotherms Studies of Equilibrium Sorption of Zn^{2+} Unto Phosphoric Acid Modified Rice Husk. *IOSR J. Appl. Chem. IOSR JAC* **2012**, *3*, 38–45. [CrossRef]
8. Chhetri, T.; Cunningham, G.; Suresh, D.; Shanks, B.; Kannan, R.; Upendran, A.; Afrasiabi, Z. Wastewater Treatment Using Novel Magnetic Nanosponges. *Water* **2022**, *14*, 505. [CrossRef]
9. Santos, T.R.T.; Silva, M.F.; Nishi, L.; Vieira, A.M.S.; Klein, M.R.F.; Andrade, M.B.; Vieira, M.F.; Bergamasco, R. Development of a Magnetic Coagulant Based on Moringa Oleifera Seed Extract for Water Treatment. *Environ. Sci. Pollut. Res.* **2016**, *23*, 7692–7700. [CrossRef]
10. Yusop, M.F.M.; Ahmad, M.A.; Rosli, N.A.; Manaf, M.E.A. Adsorption of Cationic Methylene Blue Dye Using Microwave-Assisted Activated Carbon Derived from Acacia Wood: Optimization and Batch Studies. *Arab. J. Chem.* **2021**, *14*, 103122. [CrossRef]
11. Khan, I.; Saeed, K.; Zekker, I.; Zhang, B.; Hendi, A.H.; Ahmad, A.; Ahmad, S.; Zada, N.; Ahmad, H.; Shah, L.A.; et al. Review on Methylene Blue: Its Properties, Uses, Toxicity and Photodegradation. *Water* **2022**, *14*, 242. [CrossRef]
12. Strobel, R.; Pratsinis, S.E. Direct Synthesis of Maghemite, Magnetite and Wustite Nanoparticles by Flame Spray Pyrolysis. *Adv. Powder Technol.* **2009**, *20*, 190–194. [CrossRef]
13. Machala, L.; Zboril, R.; Gedanken, A. Amorphous Iron(III) OxideA Review. *J. Phys. Chem. B* **2007**, *111*, 4003–4018. [CrossRef]
14. Ma, J.; Jing, Y.; Gao, L.; Chen, J.; Wang, Z.; Weng, L.; Li, H.; Chen, Y.; Li, Y. Hetero-Aggregation of Goethite and Ferrihydrite Nanoparticles Controlled by Goethite Nanoparticles with Elongated Morphology. *Sci. Total Environ.* **2020**, *748*, 141536. [CrossRef] [PubMed]
15. Can, M.M.; Coşkun, M.; Fırat, T. A Comparative Study of Nanosized Iron Oxide Particles; Magnetite (Fe_3O_4), Maghemite (γ-Fe_2O_3) and Hematite (α-Fe_2O_3), Using Ferromagnetic Resonance. *J. Alloys Compd.* **2012**, *542*, 241–247. [CrossRef]
16. Seabra, A.B.; Pelegrino, M.T.; Haddad, P.S. Antimicrobial Applications of Superparamagnetic Iron Oxide Nanoparticles. In *Nanostructures for Antimicrobial Therapy*; Elsevier: Amsterdam, The Netherlands, 2017; pp. 531–550, ISBN 978-0-323-46152-8.
17. Wahajuddin; Arora, S. Superparamagnetic Iron Oxide Nanoparticles: Magnetic Nanoplatforms as Drug Carriers. *Int. J. Nanomed.* **2012**, *7*, 3445–3471. [CrossRef]
18. Jabbar, K.Q.; Barzinjy, A.A.; Hamad, S.M. Iron Oxide Nanoparticles: Preparation Methods, Functions, Adsorption and Coagulation/Flocculation in Wastewater Treatment. *Environ. Nanotechnol. Monit. Manag.* **2022**, *17*, 100661. [CrossRef]
19. Caruntu, D.; Caruntu, G.; O'Connor, C.J. Magnetic Properties of Variable-Sized Fe_3O_4 Nanoparticles Synthesized from Non-Aqueous Homogeneous Solutions of Polyols. *J. Phys. D Appl. Phys.* **2007**, *40*, 5801–5809. [CrossRef]
20. Ejderyan, N.; Sanyal, R.; Sanyal, A. Chapter 6—Stimuli-Responsive Polymer-Coated Iron Oxide Nanoparticles as Drug Delivery Platforms. In *Stimuli-Responsive Nanocarriers*; Gajbhiye, V., Gajbhiye, K.R., Hong, S., Eds.; Academic Press: Cambridge, MA, USA, 2022; pp. 133–169, ISBN 978-0-12-824456-2.
21. Basuki, J.S.; Jacquemin, A.; Esser, L.; Li, Y.; Boyer, C.; Davis, T.P. A Block Copolymer-Stabilized Co-Precipitation Approach to Magnetic Iron Oxide Nanoparticles for Potential Use as MRI Contrast Agents. *Polym. Chem.* **2014**, *5*, 2611–2620. [CrossRef]
22. Herranz, F.; Salinas, B.; Groult, H.; Pellico, J.; Lechuga-Vieco, A.V.; Bhavesh, R.; Ruiz-Cabello, J. Superparamagnetic Nanoparticles for Atherosclerosis Imaging. *Nanomaterials* **2014**, *4*, 408–438. [CrossRef]
23. Jensen, K.M.Ø.; Andersen, H.L.; Tyrsted, C.; Bøjesen, E.D.; Dippel, A.-C.; Lock, N.; Billinge, S.J.L.; Iversen, B.B.; Christensen, M. Mechanisms for Iron Oxide Formation under Hydrothermal Conditions: An in Situ Total Scattering Study. *ACS Nano* **2014**, *8*, 10704–10714. [CrossRef]
24. Kurzhals, S.; Zirbs, R.; Reimhult, E. Synthesis and Magneto-Thermal Actuation of Iron Oxide Core–PNIPAM Shell Nanoparticles. *ACS Appl. Mater. Interfaces* **2015**, *7*, 19342–19352. [CrossRef]
25. Chin, A.B.; Yaacob, I.I. Synthesis and Characterization of Magnetic Iron Oxide Nanoparticles via w/o Microemulsion and Massart's Procedure. *J. Mater. Process. Technol.* **2007**, *191*, 235–237. [CrossRef]
26. Wang, J.; Sun, J.; Sun, Q.; Chen, Q. One-Step Hydrothermal Process to Prepare Highly Crystalline Fe_3O_4 Nanoparticles with Improved Magnetic Properties. *Mater. Res. Bull.* **2003**, *38*, 1113–1118. [CrossRef]
27. Mao, B.; Kang, Z.; Wang, E.; Lian, S.; Gao, L.; Tian, C.; Wang, C. Synthesis of Magnetite Octahedrons from Iron Powders through a Mild Hydrothermal Method. *Mater. Res. Bull.* **2006**, *41*, 2226–2231. [CrossRef]
28. Sun, S.; Zeng, H. Size-Controlled Synthesis of Magnetite Nanoparticles. *J. Am. Chem. Soc.* **2002**, *124*, 8204–8205. [CrossRef]

29. Lassenberger, A.; Grünewald, T.A.; van Oostrum, P.D.J.; Rennhofer, H.; Amenitsch, H.; Zirbs, R.; Lichtenegger, H.C.; Reimhult, E. Monodisperse Iron Oxide Nanoparticles by Thermal Decomposition: Elucidating Particle Formation by Second-Resolved in Situ Small-Angle X-Ray Scattering. *Chem. Mater.* **2017**, *29*, 4511–4522. [CrossRef] [PubMed]
30. Park, J.; An, K.; Hwang, Y.; Park, J.-G.; Noh, H.-J.; Kim, J.-Y.; Park, J.-H.; Hwang, N.-M.; Hyeon, T. Ultra-Large-Scale Syntheses of Monodisperse Nanocrystals. *Nat. Mater.* **2004**, *3*, 891–895. [CrossRef]
31. Guardia, P.; Pérez-Juste, J.; Labarta, A.; Batlle, X.; Liz-Marzán, L.M. Heating Rate Influence on the Synthesis of Iron Oxide Nanoparticles: The Case of Decanoic Acid. *Chem. Commun.* **2010**, *46*, 6108–6110. [CrossRef]
32. Doan, L.; Lu, Y.; Karatela, M.; Phan, V.; Jeffryes, C.; Benson, T.; Wujcik, E.K. Surface Modifications of Superparamagnetic Iron Oxide Nanoparticles with Polylactic Acid-Polyethylene Glycol Diblock Copolymer and Graphene Oxide for a Protein Delivery Vehicle. *Eng. Sci.* **2019**, *7*, 10–16. [CrossRef]
33. Doan, L.; Nguyen, L.T.; Nguyen, N.T.N. Modifying Superparamagnetic Iron Oxides Nanoparticles for Doxorubicin Delivery Carriers: A Review. *J. Nanopart. Res.* **2023**, *25*, 73. [CrossRef]
34. Marinin, A. Synthesis and Characterization of Superparamagnetic Iron Oxide Nanoparticles Coated with Silica. Master's Thesis, Royal Institute of Technology, Stockholm, Sweden, 2012.
35. Riaz, S.; Bashir, M.; Naseem, S. Iron Oxide Nanoparticles Prepared by Modified Co-Precipitation Method. *IEEE Trans. Magn.* **2014**, *50*, 40105586. [CrossRef]
36. Kang, Y.S.; Risbud, S.; Rabolt, J.F.; Stroeve, P. Synthesis and Characterization of Nanometer-Size Fe_3O_4 and γ-Fe_2O_3 Particles. *Chem. Mater.* **1996**, *8*, 2209–2211. [CrossRef]
37. Bruce, I.J.; Taylor, J.; Todd, M.; Davies, M.J.; Borioni, E.; Sangregorio, C.; Sen, T. Synthesis, Characterisation and Application of Silica-Magnetite Nanocomposites. *J. Magn. Magn. Mater.* **2004**, *284*, 145–160. [CrossRef]
38. Laurent, S.; Forge, D.; Port, M.; Roch, A.; Robic, C.; Vander Elst, L.; Muller, R.N. Magnetic Iron Oxide Nanoparticles: Synthesis, Stabilization, Vectorization, Physicochemical Characterizations, and Biological Applications. *Chem. Rev.* **2008**, *108*, 2064–2110. [CrossRef]
39. Gupta, A.K.; Curtis, A.S.G. Lactoferrin and Ceruloplasmin Derivatized Superparamagnetic Iron Oxide Nanoparticles for Targeting Cell Surface Receptors. *Biomaterials* **2004**, *25*, 3029–3040. [CrossRef] [PubMed]
40. Kim, D.K.; Zhang, Y.; Voit, W.; Rao, K.V.; Muhammed, M. Synthesis and Characterization of Surfactant-Coated Superparamagnetic Monodispersed Iron Oxide Nanoparticles. *J. Magn. Magn. Mater.* **2001**, *225*, 30–36. [CrossRef]
41. Zhu, N.; Ji, H.; Yu, P.; Niu, J.; Farooq, M.; Akram, M.; Udego, I.; Li, H.; Niu, X. Surface Modification of Magnetic Iron Oxide Nanoparticles. *Nanomaterials* **2018**, *8*, 810. [CrossRef]
42. Massart, R.; Cabuil, V. Effect of some parameters on the formation of colloidal magnetite in alkaline-medium-yield and particle-size control. *J. Chim. Phys. Phys. Chim. Biol.* **1987**, *84*, 967–973. [CrossRef]
43. Muthiah, M.; Park, I.-K.; Cho, C.-S. Surface Modification of Iron Oxide Nanoparticles by Biocompatible Polymers for Tissue Imaging and Targeting. *Biotechnol. Adv.* **2013**, *31*, 1224–1236. [CrossRef]
44. Hadjipanayis, G.C.; Siegel, R.W. (Eds.) *Nanophase Materials*; Springer: Dordrecht, The Netherlands, 1994; ISBN 978-94-010-4469-1.
45. Sjøgren, C.E.; Briley-Saebø, K.; Hanson, M.; Johansson, C. Magnetic Characterization of Iron Oxides for Magnetic Resonance Imaging. *Magn. Reson. Med.* **1994**, *31*, 268–272. [CrossRef] [PubMed]
46. Tartaj, P.; Morales, M.P.; Veintemillas-Verdaguer, S.; Gonzalez-Carreño, T.; Serna, C.J. Chapter 5 Synthesis, Properties and Biomedical Applications of Magnetic Nanoparticles. In *Handbook of Magnetic Materials*; Elsevier: Amsterdam, The Netherlands, 2006; Volume 16, pp. 403–482, ISBN 978-0-444-51850-7.
47. Hyeon, T.; Lee, S.S.; Park, J.; Chung, Y.; Na, H.B. Synthesis of Highly Crystalline and Monodisperse Maghemite Nanocrystallites without a Size-Selection Process. *J. Am. Chem. Soc.* **2001**, *123*, 12798–12801. [CrossRef]
48. Chen, D.; Xu, R. Hydrothermal Synthesis and Characterization of Nanocrystalline Fe_3O_4 Powders. *Mater. Res. Bull.* **1998**, *33*, 1015–1021. [CrossRef]
49. Sato, S.; Murakata, T.; Yanagi, H.; Miyasaka, F.; Iwaya, S. Hydrothermal Synthesis of Fine Perovskite PbTiO3 Powders with a Simple Mode of Size Distribution. *J. Mater. Sci.* **1994**, *29*, 5657–5663. [CrossRef]
50. Park, J.; Lee, E.; Hwang, N.-M.; Kang, M.; Kim, S.C.; Hwang, Y.; Park, J.-G.; Noh, H.-J.; Kim, J.-Y.; Park, J.-H.; et al. One-Nanometer-Scale Size-Controlled Synthesis of Monodisperse Magnetic Iron Oxide Nanoparticles. *Angew. Chem. Int. Ed.* **2005**, *44*, 2872–2877. [CrossRef]
51. Dai, Z.; Meiser, F.; Möhwald, H. Nanoengineering of Iron Oxide and Iron Oxide/Silica Hollow Spheres by Sequential Layering Combined with a Sol–Gel Process. *J. Colloid Interface Sci.* **2005**, *288*, 298–300. [CrossRef] [PubMed]
52. Durães, L.; Costa, B.F.O.; Vasques, J.; Campos, J.; Portugal, A. Phase Investigation of As-Prepared Iron Oxide/Hydroxide Produced by Sol–Gel Synthesis. *Mater. Lett.* **2005**, *59*, 859–863. [CrossRef]
53. Ismail, A.A. Synthesis and Characterization of $Y_2O_3/Fe_2O_3/TiO_2$ Nanoparticles by Sol–Gel Method. *Appl. Catal. B Environ.* **2005**, *58*, 115–121. [CrossRef]
54. Liu, X.Q.; Tao, S.W.; Shen, Y.S. Preparation and Characterization of Nanocrystalline α-Fe_2O_3 by a Sol-Gel Process. *Sens. Actuators B Chem.* **1997**, *40*, 161–165. [CrossRef]
55. Kojima, K.; Miyazaki, M.; Mizukami, F.; Maeda, K. Selective Formation of Spinel Iron Oxide in Thin Films by Complexing Agent-Assisted Sol-Gel Processing. *J. Sol Gel Sci. Technol.* **1997**, *8*, 77–81. [CrossRef]

56. Cannas, C.; Gatteschi, D.; Musinu, A.; Piccaluga, G.; Sangregorio, C. Structural and Magnetic Properties of Fe_2O_3 Nanoparticles Dispersed over a Silica Matrix. *J. Phys. Chem. B* **1998**, *102*, 7721–7726. [CrossRef]
57. Ennas, G.; Musinu, A.; Piccaluga, G.; Zedda, D.; Gatteschi, D.; Sangregorio, C.; Stanger, J.L.; Concas, G.; Spano, G. Characterization of Iron Oxide Nanoparticles in an $Fe_2O_3-SiO_2$ Composite Prepared by a Sol−Gel Method. *Chem. Mater.* **1998**, *10*, 495–502. [CrossRef]
58. da Costa, G.M.; De Grave, E.; de Bakker, P.M.A.; Vandenberghe, R.E. Synthesis and Characterization of Some Iron Oxides by Sol-Gel Method. *J. Solid State Chem.* **1994**, *113*, 405–412. [CrossRef]
59. del Monte, F.; Morales, M.P.; Levy, D.; Fernandez, A.; Ocaña, M.; Roig, A.; Molins, E.; O'Grady, K.; Serna, C.J. Formation of γ-Fe_2O_3 Isolated Nanoparticles in a Silica Matrix. *Langmuir* **1997**, *13*, 3627–3634. [CrossRef]
60. Chanéac, C.; Tronc, E.; Jolivet, J.P. Thermal Behavior of Spinel Iron Oxide-Silica Composites. *Nanostruct. Mater.* **1995**, *6*, 715–718. [CrossRef]
61. Niznansky, D.; Rehspringer, J.L.; Drillon, M. Preparation of Magnetic Nanoparticles (/Spl Gamma/-Fe/Sub_2/O/Sub_3/) in the Silica Matrix. *IEEE Trans. Magn.* **1994**, *30*, 821–823. [CrossRef]
62. Bentivegna, F.; Nyvlt, M.; Ferré, J.; Jamet, J.P.; Brun, A.; Visnovsky, S.; Urban, R. Magnetically Textured γ-Fe_2O_3 Nanoparticles in a Silica Gel Matrix: Optical and Magneto-Optical Properties. *J. Appl. Phys.* **1999**, *85*, 2270–2278. [CrossRef]
63. Solinas, S.; Piccaluga, G.; Morales, M.P.; Serna, C.J. Sol-Gel Formation of γ-Fe_2O_3/SiO_2 Nanocomposites. *Acta Mater.* **2001**, *49*, 2805–2811. [CrossRef]
64. Fievet, F.; Lagier, J.P.; Blin, B.; Beaudoin, B.; Figlarz, M. Homogeneous and Heterogeneous Nucleations in the Polyol Process for the Preparation of Micron and Submicron Size Metal Particles. *Solid State Ion.* **1989**, *32–33*, 198–205. [CrossRef]
65. Tzitzios, V.K.; Petridis, D.; Zafiropoulou, I.; Hadjipanayis, G.; Niarchos, D. Synthesis and Characterization of L10 FePt Nanoparticles from Pt–Fe_3O_4 Core-Shell Nanoparticles. *J. Magn. Magn. Mater.* **2005**, *294*, e95–e98. [CrossRef]
66. Chow, G.M.; Kurihara, L.K.; Kemner, K.M.; Schoen, P.E.; Elam, W.T.; Ervin, A.; Keller, S.; Zhang, Y.D.; Budnick, J.; Ambrose, T. Structural, Morphological, and Magnetic Study of Nanocrystalline Cobalt-Copper Powders Synthesized by the Polyol Process. *J. Mater. Res.* **1995**, *10*, 1546–1554. [CrossRef]
67. Viau, G.; Ravel, F.; Acher, O.; Fiévet-Vincent, F.; Fiévet, F. Preparation and Microwave Characterization of Spherical and Monodisperse $Co_{20}Ni_{80}$ Particles. *J. Appl. Phys.* **1994**, *76*, 6570–6572. [CrossRef]
68. Viau, G.; Ravel, F.; Acher, O.; Fiévet-Vincent, F.; Fiévet, F. Preparation and Microwave Characterization of Spherical and Monodisperse CoNi Particles. *J. Magn. Magn. Mater.* **1995**, *140–144*, 377–378. [CrossRef]
69. Viau, G.; Fiévet-Vincent, F.; Fiévet, F. Monodisperse Iron-Based Particles: Precipitation in Liquid Polyols. *J. Mater. Chem.* **1996**, *6*, 1047–1053. [CrossRef]
70. Viau, G.; Fiévet-Vincent, F.; Fiévet, F. Nucleation and Growth of Bimetallic CoNi and FeNi Monodisperse Particles Prepared in Polyols. *Solid State Ion.* **1996**, *84*, 259–270. [CrossRef]
71. Viau, G.; Fiévet-Vincent, F.; Fiévet, F.; Toneguzzo, P.; Ravel, F.; Acher, O. Size Dependence of Microwave Permeability of Spherical Ferromagnetic Particles. *J. Appl. Phys.* **1997**, *81*, 2749–2754. [CrossRef]
72. Toneguzzo, P.; Acher, O.; Viau, G.; Fiévet-Vincent, F.; Fiévet, F. Observations of Exchange Resonance Modes on Submicrometer Sized Ferromagnetic Particles. *J. Appl. Phys.* **1997**, *81*, 5546–5548. [CrossRef]
73. Toneguzzo, P.; Viau, G.; Acher, O.; Fiévet-Vincent, F.; Fiévet, F. Monodisperse Ferromagnetic Particles for Microwave Applications. *Adv. Mater.* **1998**, *10*, 1032–1035. [CrossRef]
74. Toneguzzo, P.; Acher, O.; Viau, G.; Pierrard, A.; Fievet-Vincent, F.; Fievet, F.; Rosenman, I. Static and Dynamic Magnetic Properties of Fine CoNi and FeCoNi Particles Synthesized by the Polyol Process. *IEEE Trans. Magn.* **1999**, *35*, 3469–3471. [CrossRef]
75. Yu, S.; Chow, G.M. Synthesis of Monodisperse Iron Oxide and Iron/Iron Oxide Core/Shell Nanoparticles via Iron-Oleylamine Complex. *J. Nanosci. Nanotechnol.* **2006**, *6*, 2135–2140. [CrossRef]
76. Hegde, M.S.; Larcher, D.; Dupont, L.; Beaudoin, B.; Tekaia-Elhsissen, K.; Tarascon, J.-M. Synthesis and Chemical Reactivity of Polyol Prepared Monodisperse Nickel Powders. *Solid State Ion.* **1996**, *93*, 33–50. [CrossRef]
77. Saravanan, P.; Jose, T.A.; Thomas, P.J.; Kulkarni, G.U. Submicron Particles of Co, Ni and Co-Ni Alloys. *Bull. Mater. Sci.* **2001**, *24*, 515–521. [CrossRef]
78. Jungk, H.-O.; Feldmann, C. Nonagglomerated, Submicron α–Fe_2O_3 Particles: Preparation and Application. *J. Mater. Res.* **2000**, *15*, 2244–2248. [CrossRef]
79. Feldmann, C. Preparation of Nanoscale Pigment Particles. *Adv. Mater.* **2001**, *13*, 1301–1303. [CrossRef]
80. Bianco, A.; Gusmano, G.; Montanari, R.; Montesperelli, G.; Traversa, E. Preparation of NiCo Metal Powders by Co-Reduction of Ni(II) and Co(II) Hydroxides for Magnetoresistive Sensors. *Mater. Lett.* **1994**, *19*, 263–268. [CrossRef]
81. Bianco, A.; Gusmano, G.; Montanari, R.; Montesperelli, G.; Traversa, E. Microstructural Characterisation of Ni, Co and Ni-Co Fine Powders for Physical Sensors. *Thermochim. Acta* **1995**, *269–270*, 117–132. [CrossRef]
82. Kurihara, L.K.; Chow, G.M.; Schoen, P.E. Nanocrystalline Metallic Powders and Films Produced by the Polyol Method. *Nanostruct. Mater.* **1995**, *5*, 607–613. [CrossRef]
83. Ammar, S.; Helfen, A.; Jouini, N.; Fiévet, F.; Rosenman, I.; Villain, F.; Molinié, P.; Danot, M. Magnetic Properties of Ultrafine Cobalt Ferrite Particles Synthesized by Hydrolysis in a Polyol MediumBasis of a Presentation given at Materials Discussion No. 3, 26–29 September, 2000, University of Cambridge, UK. *J. Mater. Chem.* **2001**, *11*, 186–192. [CrossRef]

84. Yu, W.; Wang, Y.; Liu, H.; Zheng, W. Preparation and Characterization of Polymer-Protected PtCo Bimetallic Colloids and Their Catalytic Properties in the Selective Hydrogenation of Cinnamaldehyde. *J. Mol. Catal. A Chem.* **1996**, *112*, 105–113. [CrossRef]
85. Kooli, F.; Rives, V.; Jones, W. Reduction of Ni2+−Al3+ and Cu2+−Al3+ Layered Double Hydroxides to Metallic Ni0 and Cu0 via Polyol Treatment. *Chem. Mater.* **1997**, *9*, 2231–2235. [CrossRef]
86. Yamaguchi, T.; Kitajima, K. Reduction of Interlayer Co2+ Ions in Fluorine Mica Using Diethylene Glycol. *J. Mater. Sci.* **1998**, *33*, 653–657. [CrossRef]
87. Toneguzzo, P.; Viau, G.; Acher, O.; Guillet, F.; Bruneton, E.; Fievet-Vincent, F.; Fievet, F. CoNi and FeCoNi Fine Particles Prepared by the Polyol Process: Physico-Chemical Characterization and Dynamic Magnetic Properties. *J. Mater. Sci.* **2000**, *35*, 3767–3784. [CrossRef]
88. Poul, L.; Jouini, N.; Fiévet, F. Layered Hydroxide Metal Acetates (Metal = Zinc, Cobalt, and Nickel): Elaboration via Hydrolysis in Polyol Medium and Comparative Study. *Chem. Mater.* **2000**, *12*, 3123–3132. [CrossRef]
89. Wu, M.; He, H.; Zhao, Z.; Yao, X. Preparation of Magnetic Cobalt Fibres and Their Microwave Properties. *J. Phys. D Appl. Phys.* **2000**, *33*, 2927–2930. [CrossRef]
90. Elumalai, P.; Vasan, H.N.; Verelst, M.; Lecante, P.; Carles, V.; Tailhades, P. Synthesis and Characterization of Sub-Micron Size Co–Ni Alloys Using Malonate as Precursor. *Mater. Res. Bull.* **2002**, *37*, 353–363. [CrossRef]
91. Teranishi, T.; Miyake, M. Novel Synthesis of Monodispersed Pd/Ni Nanoparticles. *Chem. Mater.* **1999**, *11*, 3414–3416. [CrossRef]
92. Jézéquel, D.; Guenot, J.; Jouini, N.; Fiévet, F. Submicrometer Zinc Oxide Particles: Elaboration in Polyol Medium and Morphological Characteristics. *J. Mater. Res.* **1995**, *10*, 77–83. [CrossRef]
93. Cai, W.; Wan, J. Facile Synthesis of Superparamagnetic Magnetite Nanoparticles in Liquid Polyols. *J. Colloid Interface Sci.* **2007**, *305*, 366–370. [CrossRef]
94. Sra, A.K.; Ewers, T.D.; Schaak, R.E. Direct Solution Synthesis of Intermetallic AuCu and AuCu3 Nanocrystals and Nanowire Networks. *Chem. Mater.* **2005**, *17*, 758–766. [CrossRef]
95. Joseyphus, R.J.; Kodama, D.; Matsumoto, T.; Sato, Y.; Jeyadevan, B.; Tohji, K. Role of Polyol in the Synthesis of Fe Particles. *J. Magn. Magn. Mater.* **2007**, *310*, 2393–2395. [CrossRef]
96. Pascal, C.; Pascal, J.L.; Favier, F.; Elidrissi Moubtassim, M.L.; Payen, C. Electrochemical Synthesis for the Control of γ-Fe_2O_3 Nanoparticle Size. Morphology, Microstructure, and Magnetic Behavior. *Chem. Mater.* **1999**, *11*, 141–147. [CrossRef]
97. Khan, H.R.; Petrikowski, K. Anisotropic Structural and Magnetic Properties of Arrays of $Fe_{26}Ni_{74}$ Nanowires Electrodeposited in the Pores of Anodic Alumina. *J. Magn. Magn. Mater.* **2000**, *215–216*, 526–528. [CrossRef]
98. Fürstner, A. (Ed.) *Active Metals: Preparation, Characterization, Applications*; VCH: Weinheim, Germany; New York, NY, USA, 1996; ISBN 978-3-527-29207-3.
99. Samrot, A.V.; Ali, H.H.; Selvarani, J.; Faradjeva, E.; Raji, P.; Prakash, P. Adsorption Efficiency of Chemically Synthesized Superparamagnetic Iron Oxide Nanoparticles (SPIONs) on Crystal Violet Dye. *Curr. Res. Green Sustain. Chem.* **2021**, *4*, 100066. [CrossRef]
100. Li, L.; Duan, H.; Wang, X.; Luo, C. Fabrication of Novel Magnetic Nanocomposite with a Number of Adsorption Sites for the Removal of Dye. *Int. J. Biol. Macromol.* **2015**, *78*, 17–22. [CrossRef]
101. Pandey, N.; Surana, S.; Shukla, S.K.; Singh, N.B. Methylene Blue Removal on Nano-Fe_3O_4/Poly(Vinyl Alcohol)/Polyacrylamide Hydrogel. *Emerg. Mater. Res.* **2017**, *6*, 305–313. [CrossRef]
102. Zhang, X.; Li, Y.; He, Y.; Kong, D.; Klein, B.; Yin, S.; Zhao, H. Preparation of Magnetic Activated Carbon by Activation and Modification of Char Derived from Co-Pyrolysis of Lignite and Biomass and Its Adsorption of Heavy-Metal-Containing Wastewater. *Minerals* **2022**, *12*, 665. [CrossRef]
103. Farhana, A.; Jenifer Selvarani, A.; Samrot, A.V.; Alsrhani, A.; Raji, P.; Sahithya, C.S.; Jane Cypriyana, P.J.; Senthilkumar, P.; Ling, M.P.; Yishak, S. Utilization of Superparamagnetic Iron Oxide Nanoparticles (SPIONs) Impregnated Activated Carbon for Removal of Hexavalent Chromium. *J. Nanomater.* **2022**, *2022*, 4326939. [CrossRef]
104. Le, T.D.; Tran, L.T.; Dang, H.T.M.; Tran, T.T.H.; Tran, H.V. Graphene Oxide/Polyvinyl Alcohol/Fe_3O_4 Nanocomposite: An Efficient Adsorbent for Co(II) Ion Removal. *J. Anal. Methods Chem.* **2021**, *2021*, 6670913. [CrossRef]
105. Llenas, M.; Sandoval, S.; Costa, P.M.; Oró-Solé, J.; Lope-Piedrafita, S.; Ballesteros, B.; Al-Jamal, K.T.; Tobias, G. Microwave-Assisted Synthesis of SPION-Reduced Graphene Oxide Hybrids for Magnetic Resonance Imaging (MRI). *Nanomaterials* **2019**, *9*, 1364. [CrossRef]
106. Bertran, A.; Sandoval, S.; Oró-Solé, J.; Sánchez, À.; Tobias, G. Particle Size Determination from Magnetization Curves in Reduced Graphene Oxide Decorated with Monodispersed Superparamagnetic Iron Oxide Nanoparticles. *J. Colloid Interface Sci.* **2020**, *566*, 107–119. [CrossRef]
107. Alcalá, M.D.; Real, C. Synthesis Based on the Wet Impregnation Method and Characterization of Iron and Iron Oxide-Silica Nanocomposites. *Solid State Ion.* **2006**, *177*, 955–960. [CrossRef]
108. Gushikem, Y.; Rosatto, S.S. Metal Oxide Thin Films Grafted on Silica Gel Surfaces: Recent Advances on the Analytical Application of These Materials. *J. Braz. Chem. Soc.* **2001**, *12*, 695–705. [CrossRef]
109. Woo, K.; Hong, J.; Ahn, J.-P. Synthesis and Surface Modification of Hydrophobic Magnetite to Processible Magnetite@silica-Propylamine. *J. Magn. Magn. Mater.* **2005**, *293*, 177–181. [CrossRef]
110. van Ewijk, G.A.; Vroege, G.J.; Philipse, A.P. Convenient Preparation Methods for Magnetic Colloids. *J. Magn. Magn. Mater.* **1999**, *201*, 31–33. [CrossRef]

111. Ma, D.; Guan, J.; Dénommée, S.; Enright, G.; Veres, T.; Simard, B. Multifunctional Nano-Architecture for Biomedical Applications. *Chem. Mater.* **2006**, *18*, 1920–1927. [CrossRef]
112. Lesnikovich, A.I.; Shunkevich, T.M.; Naumenko, V.N.; Vorobyova, S.A.; Baykov, M.V. Dispersity of Magnetite in Magnetic Liquids and the Interaction with a Surfactant. *J. Magn. Magn. Mater.* **1990**, *85*, 14–16. [CrossRef]
113. Sun, Y.; Duan, L.; Guo, Z.; DuanMu, Y.; Ma, M.; Xu, L.; Zhang, Y.; Gu, N. An Improved Way to Prepare Superparamagnetic Magnetite-Silica Core-Shell Nanoparticles for Possible Biological Application. *J. Magn. Magn. Mater.* **2005**, *285*, 65–70. [CrossRef]
114. Im, S.H.; Herricks, T.; Lee, Y.T.; Xia, Y. Synthesis and Characterization of Monodisperse Silica Colloids Loaded with Superparamagnetic Iron Oxide Nanoparticles. *Chem. Phys. Lett.* **2005**, *401*, 19–23. [CrossRef]
115. Yang, H.-H.; Zhang, S.-Q.; Chen, X.-L.; Zhuang, Z.-X.; Xu, J.-G.; Wang, X.-R. Magnetite-Containing Spherical Silica Nanoparticles for Biocatalysis and Bioseparations. *Anal. Chem.* **2004**, *76*, 1316–1321. [CrossRef]
116. Xie, L.; Jiang, R.; Zhu, F.; Liu, H.; Ouyang, G. Application of Functionalized Magnetic Nanoparticles in Sample Preparation. *Anal. Bioanal. Chem.* **2014**, *406*, 377–399. [CrossRef]
117. Zhao, M.; Liu, P. Adsorption of Methylene Blue from Aqueous Solutions by Modified Expanded Graphite Powder. *Desalination* **2009**, *249*, 331–336. [CrossRef]
118. Chung, D.D.L. Review Graphite. *J. Mater. Sci.* **2002**, *37*, 1475–1489. [CrossRef]
119. Castro, C.S.; Guerreiro, M.C.; Gonçalves, M.; Oliveira, L.C.A.; Anastácio, A.S. Activated Carbon/Iron Oxide Composites for the Removal of Atrazine from Aqueous Medium. *J. Hazard. Mater.* **2009**, *164*, 609–614. [CrossRef]
120. Imamoglu, M.; Yıldız, H.; Altundag, H.; Turhan, Y. Efficient Removal of Cd(II) from Aqueous Solution by Dehydrated Hazelnut Husk Carbon. *J. Dispers. Sci. Technol.* **2015**, *36*, 284–290. [CrossRef]
121. Aygun, A.; Yenisoy-Karakas, S.; Duman, I. Production of Granular Activated Carbon from Fruit Stones and Nutshells and Evaluation of Their Physical, Chemical and Adsorption Properties. *Microporous Mesoporous Mater.* **2003**, *66*, 189–195. [CrossRef]
122. Seabra, A.B.; Paula, A.J.; de Lima, R.; Alves, O.L.; Durán, N. Nanotoxicity of Graphene and Graphene Oxide. *Chem. Res. Toxicol.* **2014**, *27*, 159–168. [CrossRef]
123. Bian, Y.; Bian, Z.-Y.; Zhang, J.-X.; Ding, A.-Z.; Liu, S.-L.; Wang, H. Effect of the Oxygen-Containing Functional Group of Graphene Oxide on the Aqueous Cadmium Ions Removal. *Appl. Surf. Sci.* **2015**, *329*, 269–275. [CrossRef]
124. Gao, P.; Liu, M.; Tian, J.; Deng, F.; Wang, K.; Xu, D.; Liu, L.; Zhang, X.; Wei, Y. Improving the Drug Delivery Characteristics of Graphene Oxide Based Polymer Nanocomposites through the "One-Pot" Synthetic Approach of Single-Electron-Transfer Living Radical Polymerization. *Appl. Surf. Sci.* **2016**, *378*, 22–29. [CrossRef]
125. Pei, S.; Cheng, H.-M. The Reduction of Graphene Oxide. *Carbon* **2012**, *50*, 3210–3228. [CrossRef]
126. Wang, G.; Shen, X.; Wang, B.; Yao, J.; Park, J. Synthesis and Characterisation of Hydrophilic and Organophilic Graphene Nanosheets. *Carbon* **2009**, *47*, 1359–1364. [CrossRef]
127. Ayazi, H.; Akhavan, O.; Raoufi, M.; Varshochian, R.; Hosseini Motlagh, N.S.; Atyabi, F. Graphene Aerogel Nanoparticles for In-Situ Loading/PH Sensitive Releasing Anticancer Drugs. *Colloids Surf. B Biointerfaces* **2020**, *186*, 110712. [CrossRef]
128. Depan, D.; Shah, J.; Misra, R.D.K. Controlled Release of Drug from Folate-Decorated and Graphene Mediated Drug Delivery System: Synthesis, Loading Efficiency, and Drug Release Response. *Mater. Sci. Eng. C* **2011**, *31*, 1305–1312. [CrossRef]
129. Ma, D.; Lin, J.; Chen, Y.; Xue, W.; Zhang, L.-M. In Situ Gelation and Sustained Release of an Antitumor Drug by Graphene Oxide Nanosheets. *Carbon* **2012**, *50*, 3001–3007. [CrossRef]
130. Konios, D.; Stylianakis, M.M.; Stratakis, E.; Kymakis, E. Dispersion Behaviour of Graphene Oxide and Reduced Graphene Oxide. *J. Colloid Interface Sci.* **2014**, *430*, 108–112. [CrossRef]
131. Akhavan, O.; Ghaderi, E. Toxicity of Graphene and Graphene Oxide Nanowalls Against Bacteria. *ACS Nano* **2010**, *4*, 5731–5736. [CrossRef] [PubMed]
132. Akhavan, O.; Ghaderi, E.; Akhavan, A. Size-Dependent Genotoxicity of Graphene Nanoplatelets in Human Stem Cells. *Biomaterials* **2012**, *33*, 8017–8025. [CrossRef] [PubMed]
133. Li, X.; Zhu, H.; Feng, J.; Zhang, J.; Deng, X.; Zhou, B.; Zhang, H.; Xue, D.; Li, F.; Mellors, N.J.; et al. One-Pot Polylol Synthesis of Graphene Decorated with Size- and Density-Tunable Fe_3O_4 Nanoparticles for Porcine Pancreatic Lipase Immobilization. *Carbon* **2013**, *60*, 488–497. [CrossRef]
134. Baaziz, W.; Truong-Phuoc, L.; Duong-Viet, C.; Melinte, G.; Janowska, I.; Papaefthimiou, V.; Ersen, O.; Zafeiratos, S.; Begin, D.; Begin-Colin, S.; et al. Few Layer Graphene Decorated with Homogeneous Magnetic Fe3O4 Nanoparticles with Tunable Covering Densities. *J. Mater. Chem. A* **2014**, *2*, 2690. [CrossRef]
135. Wang, Z.; Liu, C.-J. Preparation and Application of Iron Oxide/Graphene Based Composites for Electrochemical Energy Storage and Energy Conversion Devices: Current Status and Perspective. *Nano Energy* **2015**, *11*, 277–293. [CrossRef]
136. Xu, C.; Sun, S. New Forms of Superparamagnetic Nanoparticles for Biomedical Applications. *Adv. Drug Deliv. Rev.* **2013**, *65*, 732–743. [CrossRef]
137. Mekonnen, T.W.; Birhan, Y.S.; Andrgie, A.T.; Hanurry, E.Y.; Darge, H.F.; Chou, H.-Y.; Lai, J.-Y.; Tsai, H.-C.; Yang, J.M.; Chang, Y.-H. Encapsulation of Gadolinium Ferrite Nanoparticle in Generation 4.5 Poly(Amidoamine) Dendrimer for Cancer Theranostics Applications Using Low Frequency Alternating Magnetic Field. *Colloids Surf. B Biointerfaces* **2019**, *184*, 110531. [CrossRef] [PubMed]

138. Morawski, A.M.; Winter, P.M.; Crowder, K.C.; Caruthers, S.D.; Fuhrhop, R.W.; Scott, M.J.; Robertson, J.D.; Abendschein, D.R.; Lanza, G.M.; Wickline, S.A. Targeted Nanoparticles for Quantitative Imaging of Sparse Molecular Epitopes with MRI. *Magn. Reson. Med.* **2004**, *51*, 480–486. [CrossRef] [PubMed]
139. Shepherd, P.G.; Popplewell, J.; Charles, S.W. A Method of Producing Ferrofluid with Gadolinium Particles. *J. Phys. D Appl. Phys.* **1970**, *3*, 1985–1986. [CrossRef]
140. Xu, H.K.; Sorensen, C.M.; Klabunde, K.J.; Hadjipanayis, G.C. Aerosol Synthesis of Gadolinium Iron Garnet Particles. *J. Mater. Res.* **1992**, *7*, 712–716. [CrossRef]
141. Arora, H.C.; Jensen, M.P.; Yuan, Y.; Wu, A.; Vogt, S.; Paunesku, T.; Woloschak, G.E. Nanocarriers Enhance Doxorubicin Uptake in Drug-Resistant Ovarian Cancer Cells. *Cancer Res.* **2012**, *72*, 769–778. [CrossRef]
142. Lyon, J.L.; Fleming, D.A.; Stone, M.B.; Schiffer, P.; Williams, M.E. Synthesis of Fe Oxide Core/Au Shell Nanoparticles by Iterative Hydroxylamine Seeding. *Nano Lett.* **2004**, *4*, 719–723. [CrossRef]
143. Lin, J.; Zhou, W.; Kumbhar, A.; Wiemann, J.; Fang, J.; Carpenter, E.E.; O'Connor, C.J. Gold-Coated Iron (Fe@Au) Nanoparticles: Synthesis, Characterization, and Magnetic Field-Induced Self-Assembly. *J. Solid State Chem.* **2001**, *159*, 26–31. [CrossRef]
144. Kim, J.; Park, S.; Lee, J.E.; Jin, S.M.; Lee, J.H.; Lee, I.S.; Yang, I.; Kim, J.-S.; Kim, S.K.; Cho, M.-H.; et al. Designed Fabrication of Multifunctional Magnetic Gold Nanoshells and Their Application to Magnetic Resonance Imaging and Photothermal Therapy. *Angew. Chem.* **2006**, *118*, 7918–7922. [CrossRef]
145. Du, J.; Jing, C. Preparation of Thiol Modified Fe_3O_4@Ag Magnetic SERS Probe for PAHs Detection and Identification. *J. Phys. Chem. C* **2011**, *115*, 17829–17835. [CrossRef]
146. A DNA-Assembled Fe3O4@Ag Nanorod in Silica Matrix for Cholesterol Biosensing | SpringerLink. Available online: https://link.springer.com/article/10.1007/s11665-015-1532-z (accessed on 10 July 2023).
147. Tamaura, Y.; Takahashi, K.; Kodera, Y.; Saito, Y.; Inada, Y. Chemical Modification of Lipase with Ferromagnetic Modifier ? A Ferromagnetic-Modified Lipase. *Biotechnol. Lett.* **1986**, *8*, 877–880. [CrossRef]
148. Butterworth, M.D.; Illum, L.; Davis, S.S. Preparation of Ultrafine Silica- and PEG-Coated Magnetite Particles. *Colloids Surf. A Physicochem. Eng. Asp.* **2001**, *179*, 93–102. [CrossRef]
149. Kohler, N.; Fryxell, G.E.; Zhang, M. A Bifunctional Poly(Ethylene Glycol) Silane Immobilized on Metallic Oxide-Based Nanoparticles for Conjugation with Cell Targeting Agents. *J. Am. Chem. Soc.* **2004**, *126*, 7206–7211. [CrossRef] [PubMed]
150. Velusamy, P.; Chia-Hung, S.; Shritama, A.; Kumar, G.V.; Jeyanthi, V.; Pandian, K. Synthesis of Oleic Acid Coated Iron Oxide Nanoparticles and Its Role in Anti-Biofilm Activity against Clinical Isolates of Bacterial Pathogens. *J. Taiwan Inst. Chem. Eng.* **2016**, *59*, 450–456. [CrossRef]
151. Chang, P.R.; Yu, J.; Ma, X.; Anderson, D.P. Polysaccharides as Stabilizers for the Synthesis of Magnetic Nanoparticles. *Carbohydr. Polym.* **2011**, *83*, 640–644. [CrossRef]
152. Gaihre, B.; Khil, M.S.; Lee, D.R.; Kim, H.Y. Gelatin-Coated Magnetic Iron Oxide Nanoparticles as Carrier System: Drug Loading and in Vitro Drug Release Study. *Int. J. Pharm.* **2009**, *365*, 180–189. [CrossRef]
153. Naha, P.C.; Liu, Y.; Hwang, G.; Huang, Y.; Gubara, S.; Jonnakuti, V.; Simon-Soro, A.; Kim, D.; Gao, L.; Koo, H.; et al. Dextran-Coated Iron Oxide Nanoparticles as Biomimetic Catalysts for Localized and PH-Activated Biofilm Disruption. *ACS Nano* **2019**, *13*, 4960–4971. [CrossRef]
154. Tyukova, I.S.; Safronov, A.P.; Kotel'nikova, A.P.; Agalakova, D.Y. Electrostatic and Steric Mechanisms of Iron Oxide Nanoparticle Sol Stabilization by Chitosan. *Polym. Sci. Ser. A* **2014**, *56*, 498–504. [CrossRef]
155. Khandhar, A.P.; Keselman, P.; Kemp, S.J.; Ferguson, R.M.; Goodwill, P.W.; Conolly, S.M.; Krishnan, K.M. Evaluation of PEG-Coated Iron Oxide Nanoparticles as Blood Pool Tracers for Preclinical Magnetic Particle Imaging. *Nanoscale* **2017**, *9*, 1299–1306. [CrossRef]
156. Walker, M.; Will, I.; Pratt, A.; Chechik, V.; Genever, P.; Ungar, D. Magnetically Triggered Release of Entrapped Bioactive Proteins from Thermally Responsive Polymer-Coated Iron Oxide Nanoparticles for Stem-Cell Proliferation. *ACS Appl. Nano Mater.* **2020**, *3*, 5008–5013. [CrossRef]
157. Arsianti, M.; Lim, M.; Marquis, C.P.; Amal, R. Assembly of Polyethylenimine-Based Magnetic Iron Oxide Vectors: Insights into Gene Delivery. *Langmuir* **2010**, *26*, 7314–7326. [CrossRef]
158. Zhang, M.; O'Connor, C.J. Synthesis and Characterization of PMMA Coated Magnetite Nanocomposites by Emulsion Polymerization. *MRS Online Proc. Libr. OPL* **2007**, *1032*, 1442. [CrossRef]
159. Padwal, P.; Bandyopadhyaya, R.; Mehra, S. Polyacrylic Acid-Coated Iron Oxide Nanoparticles for Targeting Drug Resistance in Mycobacteria. *Langmuir* **2014**, *30*, 15266–15276. [CrossRef] [PubMed]
160. Jain, N.; Singh, V.K.; Chauhan, S. A Review on Mechanical and Water Absorption Properties of Polyvinyl Alcohol Based Composites/Films. *J. Mech. Behav. Mater.* **2017**, *26*, 213–222. [CrossRef]
161. Nguyen, T.T.; Phung, T.K.; Bui, X.-T.; Doan, V.-D.; Tran, T.V.; Nguyen, D.V.; Lim, K.T.; Nguyen, T.D. Removal of Cationic Dye Using Polyvinyl Alcohol Membrane Functionalized by D-Glucose and Agar. *J. Water Process Eng.* **2021**, *40*, 101982. [CrossRef]
162. Jun, L.Y.; Mubarak, N.M.; Yon, L.S.; Bing, C.H.; Khalid, M.; Jagadish, P.; Abdullah, E.C. Immobilization of Peroxidase on Functionalized MWCNTs-Buckypaper/Polyvinyl Alcohol Nanocomposite Membrane. *Sci. Rep.* **2019**, *9*, 2215. [CrossRef] [PubMed]
163. Merdas, S.; Al-Graiti, W.; Al-Ameer, A. Using PVA@WNS Composite as Adsorbent for Methylene Blue Dye from Aqueous Solutions. *J. Med. Chem. Sci.* **2022**, *5*, 1289–1298.

164. Al Naim, A.F.; El-Shamy, A.G. A New Reusable Adsorbent of Polyvinyl Alcohol/Magnesium Peroxide (PVA/MgO_2) for Highly Selective Adsorption and Dye Removal. *Mater. Chem. Phys.* **2021**, *270*, 124820. [CrossRef]
165. Yang, X.; Li, Y.; Du, Q.; Wang, X.; Hu, S.; Chen, L.; Wang, Z.; Xia, Y.; Xia, L. Adsorption of Methylene Blue from Aqueous Solutions by Polyvinyl Alcohol/Graphene Oxide Composites. *J. Nanosci. Nanotechnol.* **2016**, *16*, 1775–1782. [CrossRef]
166. Yokoi, H.; Kantoh, T. Thermal Decomposition of the Iron(III) Hydroxide and Magnetite Composites of Poly(Vinyl Alcohol). Preparation of Magnetite and Metallic Iron Particles. *Bull. Chem. Soc. Jpn.* **1993**, *66*, 1536–1541. [CrossRef]
167. Sairam, M.; Naidu, B.V.K.; Nataraj, S.K.; Sreedhar, B.; Aminabhavi, T.M. Poly(Vinyl Alcohol)-Iron Oxide Nanocomposite Membranes for Pervaporation Dehydration of Isopropanol, 1,4-Dioxane and Tetrahydrofuran. *J. Membr. Sci.* **2006**, *283*, 65–73. [CrossRef]
168. Schöpf, B.; Neuberger, T.; Schulze, K.; Petri, A.; Chastellain, M.; Hofmann, M.; Hofmann, H.; von Rechenberg, B. Methodology Description for Detection of Cellular Uptake of PVA Coated Superparamagnetic Iron Oxide Nanoparticles (SPION) in Synovial Cells of Sheep. *J. Magn. Magn. Mater.* **2005**, *293*, 411–418. [CrossRef]
169. Doondani, P.; Jugade, R.; Gomase, V.; Shekhawat, A.; Bambal, A.; Pandey, S. Chitosan/Graphite/Polyvinyl Alcohol Magnetic Hydrogel Microspheres for Decontamination of Reactive Orange 16 Dye. *Water* **2022**, *14*, 3411. [CrossRef]
170. Sekhavat Pour, Z.; Ghaemy, M. Removal of Dyes and Heavy Metal Ions from Water by Magnetic Hydrogel Beads Based on Poly(Vinyl Alcohol)/Carboxymethyl Starch-g-Poly(Vinyl Imidazole). *RSC Adv.* **2015**, *5*, 64106–64118. [CrossRef]
171. Travlou, N.A.; Kyzas, G.Z.; Lazaridis, N.K.; Deliyanni, E.A. Graphite Oxide/Chitosan Composite for Reactive Dye Removal. *Chem. Eng. J.* **2013**, *217*, 256–265. [CrossRef]
172. Bryan, M.Y.K.; Chai, P.V.; Law, J.Y.; Mahmoudi, E. Graphene Oxide-Chitosan Composite Material as Adsorbent in Removing Methylene Blue Dye from Synthetic Wastewater. *Mater. Today Proc.* **2022**, *64*, 1587–1596. [CrossRef]
173. Dissanayake, N.S.L.; Pathirana, M.A.; Wanasekara, N.D.; Nandasiri, G.K. Chitosan-Graphene Oxide Composite Membrane for Methylene Blue Removal. In Proceedings of the 2022 Moratuwa Engineering Research Conference (MERCon), Moratuwa, Sri Lanka, 27 July 2022; pp. 1–6.
174. Aranaz, I.; Alcántara, A.R.; Civera, M.C.; Arias, C.; Elorza, B.; Heras Caballero, A.; Acosta, N. Chitosan: An Overview of Its Properties and Applications. *Polymers* **2021**, *13*, 3256. [CrossRef]
175. Zhang, Y.; Du, B.; Wu, Y.; Liu, Z.; Wang, J.; Xu, J.; Tong, Z.; Mu, X.; Liu, B. Fe_3O_4@PDA@PEI Core-Shell Microspheres as a Novel Magnetic Sorbent for the Rapid and Broad-Spectrum Separation of Bacteria in Liquid Phase. *Materials* **2022**, *15*, 2039. [CrossRef]
176. Li, G.; Jiang, Y.; Huang, K.; Ding, P.; Chen, J. Preparation and Properties of Magnetic Fe_3O_4–Chitosan Nanoparticles. *J. Alloys Compd.* **2008**, *466*, 451–456. [CrossRef]
177. Amini-Fazl, M.S.; Mohammadi, R.; Kheiri, K. 5-Fluorouracil Loaded Chitosan/Polyacrylic Acid/Fe_3O_4 Magnetic Nanocomposite Hydrogel as a Potential Anticancer Drug Delivery System. *Int. J. Biol. Macromol.* **2019**, *132*, 506–513. [CrossRef]
178. Bixner, O.; Kurzhals, S.; Virk, M.; Reimhult, E. Triggered Release from Thermoresponsive Polymersomes with Superparamagnetic Membranes. *Materials* **2016**, *9*, 29. [CrossRef]
179. Shin, J.R.; An, G.S.; Choi, S.-C. Influence of Carboxylic Modification Using Polyacrylic Acid on Characteristics of Fe_3O_4 Nanoparticles with Cluster Structure. *Processes* **2021**, *9*, 1795. [CrossRef]
180. Sarkar, S.; Guibal, E.; Quignard, F.; SenGupta, A.K. Polymer-Supported Metals and Metal Oxide Nanoparticles: Synthesis, Characterization, and Applications. *J. Nanopart. Res.* **2012**, *14*, 715. [CrossRef]
181. Paul, K.G.; Frigo, T.B.; Groman, J.Y.; Groman, E.V. Synthesis of Ultrasmall Superparamagnetic Iron Oxides Using Reduced Polysaccharides. *Bioconjug. Chem.* **2004**, *15*, 394–401. [CrossRef] [PubMed]
182. Kim, D.K.; Zhang, Y.; Kehr, J.; Klason, T.; Bjelke, B.; Muhammed, M. Characterization and MRI Study of Surfactant-Coated Superparamagnetic Nanoparticles Administered into the Rat Brain. *J. Magn. Magn. Mater.* **2001**, *225*, 256–261. [CrossRef]
183. Shultz, M.D.; Calvin, S.; Fatouros, P.P.; Morrison, S.A.; Carpenter, E.E. Enhanced Ferrite Nanoparticles as MRI Contrast Agents. *J. Magn. Magn. Mater.* **2007**, *311*, 464–468. [CrossRef]
184. Cheng, J.; Zheng, Z.; Tang, W.; Shao, J.; Jiang, H.; Lin, H. A New Strategy for Stem Cells Therapy for Erectile Dysfunction: Adipose-Derived Stem Cells Transfect Neuregulin-1 Gene through Superparamagnetic Iron Oxide Nanoparticles. *Investig. Clin. Urol.* **2022**, *63*, 359–367. [CrossRef]
185. Kumar, A.; Sharma, G.; Naushad, M.; Thakur, S. SPION/β-Cyclodextrin Core–Shell Nanostructures for Oil Spill Remediation and Organic Pollutant Removal from Waste Water. *Chem. Eng. J.* **2015**, *280*, 175–187. [CrossRef]
186. Sharma, G.; Kumar, A.; Chauhan, C.; Okram, A.; Sharma, S.; Pathania, D.; Kalia, S. Pectin-Crosslinked-Guar Gum/SPION Nanocomposite Hydrogel for Adsorption of m-Cresol and o-Chlorophenol. *Sustain. Chem. Pharm.* **2017**, *6*, 96–106. [CrossRef]
187. López, J.; González-Bahamón, L.F.; Prado, J.; Caicedo, J.C.; Zambrano, G.; Gómez, M.E.; Esteve, J.; Prieto, P. Study of Magnetic and Structural Properties of Ferrofluids Based on Cobalt–Zinc Ferrite Nanoparticles. *J. Magn. Magn. Mater.* **2012**, *324*, 394–402. [CrossRef]
188. Vaidyanathan, G.; Sendhilnathan, S.; Arulmurugan, R. Structural and Magnetic Properties of Co1−xZnxFe_2O_4 Nanoparticles by Co-Precipitation Method. *J. Magn. Magn. Mater.* **2007**, *313*, 293–299. [CrossRef]
189. Tajabadi, M.; Khosroshahi, M.E.; Bonakdar, S. An Efficient Method of SPION Synthesis Coated with Third Generation PAMAM Dendrimer. *Colloids Surf. A Physicochem. Eng. Asp.* **2013**, *431*, 18–26. [CrossRef]
190. Hah, H.Y.; Gray, S.; Johnson, C.E.; Johnson, J.A.; Kolesnichenko, V.; Kucheryavy, P.; Goloverda, G. Mössbauer Spectroscopy of Superparamagnetic Fe3O4 Nanoparticles. *J. Magn. Magn. Mater.* **2021**, *539*, 168382. [CrossRef]

191. Sodipo, B.K.; Aziz, A.A. A Sonochemical Approach to the Direct Surface Functionalization of Superparamagnetic Iron Oxide Nanoparticles with (3-Aminopropyl)Triethoxysilane. *Beilstein J. Nanotechnol.* **2014**, *5*, 1472–1476. [CrossRef] [PubMed]
192. Feng, Y.; Zhou, H.; Liu, G.; Qiao, J.; Wang, J.; Lu, H.; Yang, L.; Wu, Y. Methylene Blue Adsorption onto Swede Rape Straw (*Brassica napus* L.) Modified by Tartaric Acid: Equilibrium, Kinetic and Adsorption Mechanisms. *Bioresour. Technol.* **2012**, *125*, 138–144. [CrossRef] [PubMed]
193. Kyzas, G.Z.; Lazaridis, N.K.; Mitropoulos, A.C. Removal of Dyes from Aqueous Solutions with Untreated Coffee Residues as Potential Low-Cost Adsorbents: Equilibrium, Reuse and Thermodynamic Approach. *Chem. Eng. J.* **2012**, *189*, 148–159. [CrossRef]
194. Fang, C.; Kievit, F.M.; Veiseh, O.; Stephen, Z.R.; Wang, T.; Lee, D.; Ellenbogen, R.G.; Zhang, M. Fabrication of Magnetic Nanoparticles with Controllable Drug Loading and Release through a Simple Assembly Approach. *J. Control. Release* **2012**, *162*, 233–241. [CrossRef]
195. Munnier, E.; Cohen-Jonathan, S.; Linassier, C.; Douziech-Eyrolles, L.; Marchais, H.; Soucé, M.; Hervé, K.; Dubois, P.; Chourpa, I. Novel Method of Doxorubicin–SPION Reversible Association for Magnetic Drug Targeting. *Int. J. Pharm.* **2008**, *363*, 170–176. [CrossRef]
196. Pang, K.; Sun, W.; Ye, F.; Yang, L.; Pu, M.; Yang, C.; Zhang, Q.; Niu, J. Sulfur-Modified Chitosan Derived N,S-Co-Doped Carbon as a Bifunctional Material for Adsorption and Catalytic Degradation Sulfamethoxazole by Persulfate. *J. Hazard. Mater.* **2022**, *424*, 127270. [CrossRef]
197. Gupta, A.K.; Gupta, M. Cytotoxicity Suppression and Cellular Uptake Enhancement of Surface Modified Magnetic Nanoparticles. *Biomaterials* **2005**, *26*, 1565–1573. [CrossRef]
198. Majeed, M.I.; Lu, Q.; Yan, W.; Li, Z.; Hussain, I.; Tahir, M.N.; Tremel, W.; Tan, B. Highly Water-Soluble Magnetic Iron Oxide (Fe_3O_4) Nanoparticles for Drug Delivery: Enhanced in Vitro Therapeutic Efficacy of Doxorubicin and MION Conjugates. *J. Mater. Chem. B* **2013**, *1*, 2874. [CrossRef]
199. Kayal, S.; Ramanujan, R.V. Doxorubicin Loaded PVA Coated Iron Oxide Nanoparticles for Targeted Drug Delivery. *Mater. Sci. Eng. C* **2010**, *30*, 484–490. [CrossRef]
200. An, G.S.; Chae, D.H.; Hur, J.U.; Oh, A.H.; Choi, H.-H.; Choi, S.-C.; Oh, Y.-S.; Jung, Y.-G. Hollow-Structured Fe_3O_4@SiO_2 Nanoparticles: Novel Synthesis and Enhanced Adsorbents for Purification of Plasmid DNA. *Ceram. Int.* **2018**, *44*, 18791–18795. [CrossRef]
201. Lee, H.-Y.; Lee, S.-H.; Xu, C.; Xie, J.; Lee, J.-H.; Wu, B.; Leen Koh, A.; Wang, X.; Sinclair, R.; Wang, S.X.; et al. Synthesis and Characterization of PVP-Coated Large Core Iron Oxide Nanoparticles as an MRI Contrast Agent. *Nanotechnology* **2008**, *19*, 165101. [CrossRef]
202. Kopanja, L.; Kralj, S.; Zunic, D.; Loncar, B.; Tadic, M. Core–Shell Superparamagnetic Iron Oxide Nanoparticle (SPION) Clusters: TEM Micrograph Analysis, Particle Design and Shape Analysis. *Ceram. Int.* **2016**, *42*, 10976–10984. [CrossRef]
203. Wanna, Y.; Sirapat Pratontep, S.; Pui-ngam, R.; Nukeaw, J.; Chindaduang, A.; Tumcharern, G. Preparation And Characterization of PEG Bis(Amine) Grafted PMMA/SPION Composite Nanoparticles. *Adv. Mater. Lett.* **2016**, *7*, 176–180. [CrossRef]
204. Nasrollahzadeh, M.; Atarod, M.; Sajjadi, M.; Sajadi, S.M.; Issaabadi, Z. Plant-Mediated Green Synthesis of Nanostructures: Mechanisms, Characterization, and Applications. In *Interface Science and Technology*; Elsevier: Amsterdam, The Netherlands, 2019; Volume 28, pp. 199–322, ISBN 978-0-12-813586-0.
205. Brunauer, S.; Emmett, P.H.; Teller, E. Adsorption of Gases in Multimolecular Layers. *J. Am. Chem. Soc.* **1938**, *60*, 309–319. [CrossRef]
206. Nishi, Y.; Inagaki, M. Chapter 11—Gas Adsorption/Desorption Isotherm for Pore Structure Characterization. In *Materials Science and Engineering of Carbon*; Inagaki, M., Kang, F., Eds.; Butterworth-Heinemann: Oxford, UK, 2016; pp. 227–247, ISBN 978-0-12-805256-3.
207. Barrett, E.P.; Joyner, L.G.; Halenda, P.P. The Determination of Pore Volume and Area Distributions in Porous Substances. I. Computations from Nitrogen Isotherms. *J. Am. Chem. Soc.* **1951**, *73*, 373–380. [CrossRef]
208. Kumar, K.V.; Gadipelli, S.; Wood, B.; Ramisetty, K.A.; Stewart, A.A.; Howard, C.A.; Brett, D.J.L.; Rodriguez-Reinoso, F. Characterization of the Adsorption Site Energies and Heterogeneous Surfaces of Porous Materials. *J. Mater. Chem. A* **2019**, *7*, 10104–10137. [CrossRef]
209. Yurdakal, S.; Garlisi, C.; Özcan, L.; Bellardita, M.; Palmisano, G. Chapter 4—(Photo)Catalyst Characterization Techniques: Adsorption Isotherms and BET, SEM, FTIR, UV–Vis, Photoluminescence, and Electrochemical Characterizations. In *Heterogeneous Photocatalysis*; Marcì, G., Palmisano, L., Eds.; Elsevier: Amsterdam, The Netherlands, 2019; pp. 87–152, ISBN 978-0-444-64015-4.
210. Levine, I.N. *Physical Chemistry*; Higher Education: New York, NY, USA, 2021.
211. Das, A.; Guo, H. Raman Spectroscopy. In *Reference Module in Earth Systems and Environmental Sciences*; Elsevier: Amsterdam, The Netherlands, 2022; p. B9780128229743000000, ISBN 978-0-12-409548-9.
212. de Jesús Ruíz-Baltazar, Á.; Reyes-López, S.Y.; de Lourdes Mondragón-Sánchez, M.; Robles-Cortés, A.I.; Pérez, R. Eco-Friendly Synthesis of Fe3O4 Nanoparticles: Evaluation of Their Catalytic Activity in Methylene Blue Degradation by Kinetic Adsorption Models. *Results Phys.* **2019**, *12*, 989–995. [CrossRef]
213. Papadimitriou, S.; Bikiaris, D. Novel Self-Assembled Core–Shell Nanoparticles Based on Crystalline Amorphous Moieties of Aliphatic Copolyesters for Efficient Controlled Drug Release. *J. Control. Release* **2009**, *138*, 177–184. [CrossRef]
214. Kannan, N.; Sundaram, M.M. Kinetics and Mechanism of Removal of Methylene Blue by Adsorption on Various Carbons—A Comparative Study. *Dye. Pigment.* **2001**, *51*, 25–40. [CrossRef]

215. Vimonses, V.; Lei, S.; Jin, B.; Chow, C.W.; Saint, C. Kinetic Study and Equilibrium Isotherm Analysis of Congo Red Adsorption by Clay Materials. *Chem. Eng. J.* **2009**, *148*, 354–364. [CrossRef]
216. Oladoja, N.A.; Aboluwoye, C.O.; Oladimeji, Y.B.; Ashogbon, A.O.; Otemuyiwa, I.O. Studies on Castor Seed Shell as a Sorbent in Basic Dye Contaminated Wastewater Remediation. *Desalination* **2008**, *227*, 190–203. [CrossRef]
217. Nandi, B.K.; Goswami, A.; Purkait, M.K. Removal of Cationic Dyes from Aqueous Solutions by Kaolin: Kinetic and Equilibrium Studies. *Appl. Clay Sci.* **2009**, *42*, 583–590. [CrossRef]
218. Özcan, A.S.; Erdem, B.; Özcan, A. Adsorption of Acid Blue 193 from Aqueous Solutions onto BTMA-Bentonite. *Colloids Surf. A Physicochem. Eng. Asp.* **2005**, *266*, 73–81. [CrossRef]
219. Do, T.H.; Nguyen, V.T.; Dung, N.Q.; Chu, M.N.; Van Kiet, D.; Ngan, T.T.K.; Van Tan, L. Study on Methylene Blue Adsorption of Activated Carbon Made from Moringa Oleifera Leaf. *Mater. Today Proc.* **2021**, *38*, 3405–3413. [CrossRef]
220. Cengiz, S.; Cavas, L. Removal of Methylene Blue by Invasive Marine Seaweed: Caulerpa Racemosa Var. Cylindracea. *Bioresour. Technol.* **2008**, *99*, 2357–2363. [CrossRef]
221. Yao, Y.; Xu, F.; Chen, M.; Xu, Z.; Zhu, Z. Adsorption Behavior of Methylene Blue on Carbon Nanotubes. *Bioresour. Technol.* **2010**, *101*, 3040–3046. [CrossRef]
222. Sahu, S.; Pahi, S.; Tripathy, S.; Singh, S.K.; Behera, A.; Sahu, U.K.; Patel, R.K. Adsorption of Methylene Blue on Chemically Modified Lychee Seed Biochar: Dynamic, Equilibrium, and Thermodynamic Study. *J. Mol. Liq.* **2020**, *315*, 113743. [CrossRef]
223. Sivakumar, R.; Lee, N.Y. Adsorptive Removal of Organic Pollutant Methylene Blue Using Polysaccharide-Based Composite Hydrogels. *Chemosphere* **2022**, *286*, 131890. [CrossRef]
224. Yukselen, Y.; Kaya, A. Suitability of the Methylene Blue Test for Surface Area, Cation Exchange Capacity and Swell Potential Determination of Clayey Soils. *Eng. Geol.* **2008**, *102*, 38–45. [CrossRef]
225. Ai, L.; Zhang, C.; Liao, F.; Wang, Y.; Li, M.; Meng, L.; Jiang, J. Removal of Methylene Blue from Aqueous Solution with Magnetite Loaded Multi-Wall Carbon Nanotube: Kinetic, Isotherm and Mechanism Analysis. *J. Hazard. Mater.* **2011**, *198*, 282–290. [CrossRef]
226. Oboh, I.O.; Aluyor, E.O.; Audu, T.O.K. Second-Order Kinetic Model for the Adsorption of Divalent Metal Ions on Sida Acuta Leaves. *Int. J. Phys. Sci.* **2013**, *8*, 1722–1728.
227. Sahoo, T.R.; Prelot, B. Adsorption Processes for the Removal of Contaminants from Wastewater. In *Nanomaterials for the Detection and Removal of Wastewater Pollutants*; Elsevier: Amsterdam, The Netherlands, 2020; pp. 161–222, ISBN 978-0-12-818489-9.
228. Sharma, G.; Naushad, M.; Al-Muhtaseb, A.H.; Kumar, A.; Khan, M.R.; Kalia, S.; Shweta; Bala, M.; Sharma, A. Fabrication and Characterization of Chitosan-Crosslinked-Poly(Alginic Acid) Nanohydrogel for Adsorptive Removal of Cr(VI) Metal Ion from Aqueous Medium. *Int. J. Biol. Macromol.* **2017**, *95*, 484–493. [CrossRef]
229. Sharma, G.; Kumar, A.; Devi, K.; Sharma, S.; Naushad, M.; Ghfar, A.A.; Ahamad, T.; Stadler, F.J. Guar Gum-Crosslinked-Soya Lecithin Nanohydrogel Sheets as Effective Adsorbent for the Removal of Thiophanate Methyl Fungicide. *Int. J. Biol. Macromol.* **2018**, *114*, 295–305. [CrossRef] [PubMed]
230. Sharma, G.; Kumar, A.; Naushad, M.; García-Peñas, A.; Al-Muhtaseb, A.H.; Ghfar, A.A.; Sharma, V.; Ahamad, T.; Stadler, F.J. Fabrication and Characterization of Gum Arabic-Cl-Poly(Acrylamide) Nanohydrogel for Effective Adsorption of Crystal Violet Dye. *Carbohydr. Polym.* **2018**, *202*, 444–453. [CrossRef]
231. Ma, J.; Huang, D.; Zou, J.; Li, L.; Kong, Y.; Komarneni, S. Adsorption of Methylene Blue and Orange II Pollutants on Activated Carbon Prepared from Banana Peel. *J. Porous Mater.* **2015**, *22*, 301–311. [CrossRef]
232. Langmuir, I. The Adsorption of Gases on Plane Surfaces of Glass, Mica and Platinum. *J. Am. Chem. Soc.* **1918**, *40*, 1361–1403. [CrossRef]
233. Liu, L.; Luo, X.-B.; Ding, L.; Luo, S.-L. 4—Application of Nanotechnology in the Removal of Heavy Metal From Water. In *Nanomaterials for the Removal of Pollutants and Resource Reutilization*; Micro and Nano Technologies; Luo, X., Deng, F., Eds.; Elsevier: Amsterdam, The Netherlands, 2019; pp. 83–147, ISBN 978-0-12-814837-2.
234. Bayazit, Ş.S. Magnetic Multi-Wall Carbon Nanotubes for Methyl Orange Removal from Aqueous Solutions: Equilibrium, Kinetic and Thermodynamic Studies. *Sep. Sci. Technol.* **2014**, *49*, 1389–1400. [CrossRef]
235. Ghaedi, M.; Haghdoust, S.; Kokhdan, S.N.; Mihandoost, A.; Sahraie, R.; Daneshfar, A. Comparison of Activated Carbon, Multiwalled Carbon Nanotubes, and Cadmium Hydroxide Nanowire Loaded on Activated Carbon as Adsorbents for Kinetic and Equilibrium Study of Removal of Safranine O. *Spectrosc. Lett.* **2012**, *45*, 500–510. [CrossRef]
236. Reed, B.E.; Matsumoto, M.R. Modeling Cadmium Adsorption by Activated Carbon Using the Langmuir and Freundlich Isotherm Expressions. *Sep. Sci. Technol.* **1993**, *28*, 2179–2195. [CrossRef]
237. Sheha, R.R.; Metwally, E. Equilibrium Isotherm Modeling of Cesium Adsorption onto Magnetic Materials. *J. Hazard. Mater.* **2007**, *143*, 354–361. [CrossRef] [PubMed]
238. Chabani, M.; Amrane, A.; Bensmaili, A. Kinetic Modelling of the Adsorption of Nitrates by Ion Exchange Resin. *Chem. Eng. J.* **2006**, *125*, 111–117. [CrossRef]
239. Özcan, A.; Özcan, A.S.; Tunali, S.; Akar, T.; Kiran, I. Determination of the Equilibrium, Kinetic and Thermodynamic Parameters of Adsorption of Copper(II) Ions onto Seeds of Capsicum Annuum. *J. Hazard. Mater.* **2005**, *124*, 200–208. [CrossRef]
240. Helfferich, F.G. *Ion Exchange*; Courier Corporation: North Chelmsford, MA, USA, 1995; ISBN 978-0-486-68784-1.
241. Onyango, M.S.; Kojima, Y.; Aoyi, O.; Bernardo, E.C.; Matsuda, H. Adsorption Equilibrium Modeling and Solution Chemistry Dependence of Fluoride Removal from Water by Trivalent-Cation-Exchanged Zeolite F-9. *J. Colloid Interface Sci.* **2004**, *279*, 341–350. [CrossRef]

242. Üner, O.; Geçgel, Ü.; Bayrak, Y. Adsorption of Methylene Blue by an Efficient Activated Carbon Prepared from Citrullus Lanatus Rind: Kinetic, Isotherm, Thermodynamic, and Mechanism Analysis. *Water Air Soil Pollut.* **2016**, *227*, 247. [CrossRef]
243. Hsieh, C.-T.; Teng, H. Langmuir and Dubinin-Radushkevich Analyses on Equilibrium Adsorption of Activated Carbon Fabrics in Aqueous Solutions. *J. Chem. Technol. Biotechnol.* **2000**, *75*, 1066–1072. [CrossRef]
244. Amin, N.K. Removal of Direct Blue-106 Dye from Aqueous Solution Using New Activated Carbons Developed from Pomegranate Peel: Adsorption Equilibrium and Kinetics. *J. Hazard. Mater.* **2009**, *165*, 52–62. [CrossRef]
245. Ghaedi, M.; Sadeghian, B.; Pebdani, A.A.; Sahraei, R.; Daneshfar, A.; Duran, C. Kinetics, Thermodynamics and Equilibrium Evaluation of Direct Yellow 12 Removal by Adsorption onto Silver Nanoparticles Loaded Activated Carbon. *Chem. Eng. J.* **2012**, *187*, 133–141. [CrossRef]
246. Başar, C.A. Applicability of the Various Adsorption Models of Three Dyes Adsorption onto Activated Carbon Prepared Waste Apricot. *J. Hazard. Mater.* **2006**, *135*, 232–241. [CrossRef] [PubMed]
247. Ertugay, M.; Certel, M.; Gurses, A. Moisture Adsorption Isotherms of Tarhana at 25 °C and 35 °C and the Investigation of Fitness of Various Isotherm Equations to Moisture Sorption Data of Tarhana. *J. Sci. Food Agric.* **2000**, *80*, 2001–2004. [CrossRef]
248. El Qada, E.N.; Allen, S.J.; Walker, G.M. Adsorption of Methylene Blue onto Activated Carbon Produced from Steam Activated Bituminous Coal: A Study of Equilibrium Adsorption Isotherm. *Chem. Eng. J.* **2006**, *124*, 103–110. [CrossRef]
249. Weber, W.J.; Morris, J.C. Kinetics of Adsorption on Carbon from Solution. *J. Sanit. Eng. Div.* **1963**, *89*, 31–59. [CrossRef]
250. Jawad, A.H.; Surip, S.N. Upgrading Low Rank Coal into Mesoporous Activated Carbon via Microwave Process for Methylene Blue Dye Adsorption: Box Behnken Design and Mechanism Study. *Diam. Relat. Mater.* **2022**, *127*, 109199. [CrossRef]
251. Jawad, A.H.; Ismail, K.; Ishak, M.A.M.; Wilson, L.D. Conversion of Malaysian Low-Rank Coal to Mesoporous Activated Carbon: Structure Characterization and Adsorption Properties. *Chin. J. Chem. Eng.* **2019**, *27*, 1716–1727. [CrossRef]
252. Jawad, A.H.; Mohd Firdaus Hum, N.N.; Abdulhameed, A.S.; Mohd Ishak, M.A. Mesoporous Activated Carbon from Grass Waste via H_3PO_4—Activation for Methylene Blue Dye Removal: Modelling, Optimisation, and Mechanism Study. *Int. J. Environ. Anal. Chem.* **2020**, *102*, 6061–6077. [CrossRef]
253. Tan, K.L.; Hameed, B.H. Insight into the Adsorption Kinetics Models for the Removal of Contaminants from Aqueous Solutions. *J. Taiwan Inst. Chem. Eng.* **2017**, *74*, 25–48. [CrossRef]
254. Srivastava, S.; Tyagi, R.; Pant, N. Adsorption of Heavy Metal Ions on Carbonaceous Material Developed from the Waste Slurry Generated in Local Fertilizer Plants. *Water Res.* **1989**, *23*, 1161–1165. [CrossRef]
255. Demirbas, E.; Kobya, M.; Senturk, E.; Ozkan, T. Adsorption Kinetics for the Removal of Chromium (VI) from Aqueous Solutions on the Activated Carbons Prepared from Agricultural Wastes. *Water SA* **2004**, *30*, 533–539. [CrossRef]
256. Chien, S.H.; Clayton, W.R. Application of Elovich Equation to the Kinetics of Phosphate Release and Sorption in Soils. *Soil Sci. Soc. Am. J.* **1980**, *44*, 265–268. [CrossRef]
257. Boyd, G.E.; Adamson, A.W.; Myers, L.S. The Exchange Adsorption of Ions from Aqueous Solutions by Organic Zeolites. II. Kinetics. *J. Am. Chem. Soc.* **1947**, *69*, 2836–2848. [CrossRef]
258. Hameed, B.H.; El-Khaiary, M.I. Malachite Green Adsorption by Rattan Sawdust: Isotherm, Kinetic and Mechanism Modeling. *J. Hazard. Mater.* **2008**, *159*, 574–579. [CrossRef]
259. Seki, Y.; Yurdakoç, K. Adsorption of Promethazine Hydrochloride with KSF Montmorillonite. *Adsorption* **2006**, *12*, 89–100. [CrossRef]
260. Singh, D. Studies of the Adsorption Thermodynamics of Oxamyl on Fly Ash. *Adsorpt. Sci. Technol.* **2000**, *18*, 741–748. [CrossRef]
261. Özcan, A.; Öncü, E.M.; Özcan, A.S. Kinetics, Isotherm and Thermodynamic Studies of Adsorption of Acid Blue 193 from Aqueous Solutions onto Natural Sepiolite. *Colloids Surf. A Physicochem. Eng. Asp.* **2006**, *277*, 90–97. [CrossRef]
262. Bhattacharyya, K.G.; Sharma, A. Kinetics and Thermodynamics of Methylene Blue Adsorption on Neem (Azadirachta Indica) Leaf Powder. *Dye. Pigment.* **2005**, *65*, 51–59. [CrossRef]
263. Sharma, P.; Kaur, R.; Baskar, C.; Chung, W.-J. Removal of Methylene Blue from Aqueous Waste Using Rice Husk and Rice Husk Ash. *Desalination* **2010**, *259*, 249–257. [CrossRef]
264. Karaer, H.; Kaya, İ. Synthesis, Characterization of Magnetic Chitosan/Active Charcoal Composite and Using at the Adsorption of Methylene Blue and Reactive Blue4. *Microporous Mesoporous Mater.* **2016**, *232*, 26–38. [CrossRef]
265. Srivastava, V.; Weng, C.H.; Singh, V.K.; Sharma, Y.C. Adsorption of Nickel Ions from Aqueous Solutions by Nano Alumina: Kinetic, Mass Transfer, and Equilibrium Studies. *J. Chem. Eng. Data* **2011**, *56*, 1414–1422. [CrossRef]
266. Hasan, M.; Ahmad, A.L.; Hameed, B.H. Adsorption of Reactive Dye onto Cross-Linked Chitosan/Oil Palm Ash Composite Beads. *Chem. Eng. J.* **2008**, *136*, 164–172. [CrossRef]
267. Nnadi, C.; Nwodo, N.; Obonga, W.; Uzor, P. In Vitro Adsorption Kinetic Model of Phenobarbital onto Powdered Seeds of Garcinia Kola. *Afr. J. Pharm. Pharmacol.* **2014**, *8*, 1079–1085.
268. Lazaridis, N.K.; Asouhidou, D.D. Kinetics of Sorptive Removal of Chromium(VI) from Aqueous Solutions by Calcined Mg–Al–CO_3 Hydrotalcite. *Water Res.* **2003**, *37*, 2875–2882. [CrossRef] [PubMed]
269. Özçelik, G.; Kurtulbaş Şahin, E.; Şahin, S. Effect of Ionic Strength on Methylene Blue Sorption onto Macroporous Resins: A Comprehensive Study. *J. Dispers. Sci. Technol.* **2022**, *43*, 716–725. [CrossRef]
270. Ghasemi, J.; Asadpour, S. Thermodynamics' Study of the Adsorption Process of Methylene Blue on Activated Carbon at Different Ionic Strengths. *J. Chem. Thermodyn.* **2007**, *39*, 967–971. [CrossRef]

271. Doğan, M.; Özdemir, Y.; Alkan, M. Adsorption Kinetics and Mechanism of Cationic Methyl Violet and Methylene Blue Dyes onto Sepiolite. *Dye Pigment.* **2007**, *75*, 701–713. [CrossRef]
272. Imamura, K.; Ikeda, E.; Nagayasu, T.; Sakiyama, T.; Nakanishi, K. Adsorption Behavior of Methylene Blue and Its Congeners on a Stainless Steel Surface. *J. Colloid Interface Sci.* **2002**, *245*, 50–57. [CrossRef]
273. Yazdani, O.; Irandoust, M.; Ghasemi, J.B.; Hooshmand, S. Thermodynamic Study of the Dimerization Equilibrium of Methylene Blue, Methylene Green and Thiazole Orange at Various Surfactant Concentrations and Different Ionic Strengths and in Mixed Solvents by Spectral Titration and Chemometric Analysis. *Dye. Pigment.* **2012**, *92*, 1031–1041. [CrossRef]
274. Yang, S.-T.; Chen, S.; Chang, Y.; Cao, A.; Liu, Y.; Wang, H. Removal of Methylene Blue from Aqueous Solution by Graphene Oxide. *J. Colloid Interface Sci.* **2011**, *359*, 24–29. [CrossRef] [PubMed]
275. Mahmoodi, N.M.; Hayati, B.; Arami, M.; Lan, C. Adsorption of Textile Dyes on Pine Cone from Colored Wastewater: Kinetic, Equilibrium and Thermodynamic Studies. *Desalination* **2011**, *268*, 117–125. [CrossRef]
276. Ghaedi, M.; Hassanzadeh, A.; Kokhdan, S.N. Multiwalled Carbon Nanotubes as Adsorbents for the Kinetic and Equilibrium Study of the Removal of Alizarin Red S and Morin. *J. Chem. Eng. Data* **2011**, *56*, 2511–2520. [CrossRef]
277. Salleh, M.A.M.; Mahmoud, D.K.; Karim, W.A.W.A.; Idris, A. Cationic and Anionic Dye Adsorption by Agricultural Solid Wastes: A Comprehensive Review. *Desalination* **2011**, *280*, 1–13. [CrossRef]
278. Saputra, E.; Saputra, R.; Nugraha, M.W.; Irianty, R.S.; Utama, P.S. Removal of Methylene Blue from Aqueous Solution Using Spent Bleaching Earth. *IOP Conf. Ser. Mater. Sci. Eng.* **2018**, *345*, 012008. [CrossRef]
279. Kallel, F.; Chaari, F.; Bouaziz, F.; Bettaieb, F.; Ghorbel, R.; Chaabouni, S.E. Sorption and Desorption Characteristics for the Removal of a Toxic Dye, Methylene Blue from Aqueous Solution by a Low Cost Agricultural by-Product. *J. Mol. Liq.* **2016**, *219*, 279–288. [CrossRef]
280. Noori, M.; Tahmasebpoor, M.; Foroutan, R. Enhanced Adsorption Capacity of Low-Cost Magnetic Clinoptilolite Powders/Beads for the Effective Removal of Methylene Blue: Adsorption and Desorption Studies. *Mater. Chem. Phys.* **2022**, *278*, 125655. [CrossRef]
281. Dawood, S.; Sen, T.K. Removal of Anionic Dye Congo Red from Aqueous Solution by Raw Pine and Acid-Treated Pine Cone Powder as Adsorbent: Equilibrium, Thermodynamic, Kinetics, Mechanism and Process Design. *Water Res.* **2012**, *46*, 1933–1946. [CrossRef]
282. Shahryari, Z.; Goharrizi, A.S.; Azadi, M. Experimental Study of Methylene Blue Adsorption from Aqueous Solutions onto Carbon Nano Tubes. *Int. J. Water Resour. Environ. Eng.* **2010**, *2*, 16–28.
283. Mahmoud, D.K.; Salleh, M.A.M.; Karim, W.A.W.A.; Idris, A.; Abidin, Z.Z. Batch Adsorption of Basic Dye Using Acid Treated Kenaf Fibre Char: Equilibrium, Kinetic and Thermodynamic Studies. *Chem. Eng. J.* **2012**, *181*, 449–457. [CrossRef]
284. Reddy, M.S.; Sivaramakrishna, L.; Reddy, A.V. The Use of an Agricultural Waste Material, Jujuba Seeds for the Removal of Anionic Dye (Congo Red) from Aqueous Medium. *J. Hazard. Mater.* **2012**, *203*, 118–127. [CrossRef] [PubMed]
285. Li, Z.; Sun, Y.; Xing, J.; Meng, A. Fast Removal of Methylene Blue by Fe_3O_4 Magnetic Nanoparticles and Their Cycling Property. *J. Nanosci. Nanotechnol.* **2019**, *19*, 2116–2123. [CrossRef] [PubMed]
286. Ramesh, A.V.; Rama Devi, D.; Mohan Botsa, S.; Basavaiah, K. Facile Green Synthesis of Fe_3O_4 Nanoparticles Using Aqueous Leaf Extract of Zanthoxylum Armatum DC. for Efficient Adsorption of Methylene Blue. *J. Asian Ceram. Soc.* **2018**, *6*, 145–155. [CrossRef]
287. Mohammadpour, A.; Karami, N.; Zabihi, R.; Fazeliyan, E.; Abbasi, A.; Karimi, S.; Barbosa de Farias, M.; Adeodato Vieira, M.G.; Shahsavani, E.; Mousavi Khaneghah, A. Green Synthesis, Characterization, and Application of Fe_3O_4 Nanoparticles for Methylene Blue Removal: RSM Optimization, Kinetic, Isothermal Studies, and Molecular Simulation. *Environ. Res.* **2023**, *225*, 115507. [CrossRef] [PubMed]
288. Xiang, H.; Ren, G.; Zhong, Y.; Xu, D.; Zhang, Z.; Wang, X.; Yang, X. Fe_3O_4@C Nanoparticles Synthesized by In Situ Solid-Phase Method for Removal of Methylene Blue. *Nanomaterials* **2021**, *11*, 330. [CrossRef] [PubMed]
289. Zhang, W.; Zhang, L.Y.; Zhao, X.J.; Zhou, Z. Citrus Pectin Derived Ultrasmall Fe_3O_4@C Nanoparticles as a High-Performance Adsorbent toward Removal of Methylene Blue. *J. Mol. Liq.* **2016**, *222*, 995–1002. [CrossRef]
290. Tripathy, S.; Sahu, S.; Patel, R.K.; Panda, R.B.; Kar, P.K. Novel Fe_3O_4-Modified Biochar Derived from Citrus Bergamia Peel: A Green Synthesis Approach for Adsorptive Removal of Methylene Blue. *ChemistrySelect* **2022**, *7*, e202103595. [CrossRef]
291. Habila, M.A.; Moshab, M.S.; El-Toni, A.M.; ALOthman, Z.A.; Badjah Hadj Ahmed, A.Y. Thermal Fabrication of Magnetic Fe_3O_4 (Nanoparticle)@Carbon Sheets from Waste Resources for the Adsorption of Dyes: Kinetic, Equilibrium, and UV–Visible Spectroscopy Investigations. *Nanomaterials* **2023**, *13*, 1266. [CrossRef]
292. Yao, Y.; Miao, S.; Liu, S.; Ma, L.P.; Sun, H.; Wang, S. Synthesis, Characterization, and Adsorption Properties of Magnetic Fe_3O_4@graphene Nanocomposite. *Chem. Eng. J.* **2012**, *184*, 326–332. [CrossRef]
293. Ahamad, T.; Naushad, M.; Eldesoky, G.E.; Al-Saeedi, S.I.; Nafady, A.; Al-Kadhi, N.S.; Al-Muhtaseb, A.H.; Khan, A.A.; Khan, A. Effective and Fast Adsorptive Removal of Toxic Cationic Dye (MB) from Aqueous Medium Using Amino-Functionalized Magnetic Multiwall Carbon Nanotubes. *J. Mol. Liq.* **2019**, *282*, 154–161. [CrossRef]
294. Wu, K.-H.; Huang, W.-C.; Hung, W.-C.; Tsai, C.-W. Modified Expanded Graphite/Fe_3O_4 Composite as an Adsorbent of Methylene Blue: Adsorption Kinetics and Isotherms. *Mater. Sci. Eng. B* **2021**, *266*, 115068. [CrossRef]
295. Tishbi, P.; Mosayebi, M.; Salehi, Z.; Fatemi, S.; Faegh, E. Synthesizing Magnetic Graphene Oxide Nanomaterial (GO-Fe_3O_4) and Kinetic Modelling of Methylene Blue Adsorption from Water. *Can. J. Chem. Eng.* **2022**, *100*, 3321–3334. [CrossRef]

296. Li, M.; Dong, C.; Guo, C.; Yu, L. Magnetic Activated Biochar Fe_3O_4-MOS Made from Moringa Seed Shells for the Adsorption of Methylene Blue. *Processes* **2022**, *10*, 2720. [CrossRef]
297. Xie, J.; Lin, R.; Liang, Z.; Zhao, Z.; Yang, C.; Cui, F. Effect of Cations on the Enhanced Adsorption of Cationic Dye in Fe_3O_4-Loaded Biochar and Mechanism. *J. Environ. Chem. Eng.* **2021**, *9*, 105744. [CrossRef]
298. Hingrajiya, R.D.; Patel, M.P. Fe_3O_4 Modified Chitosan Based Co-Polymeric Magnetic Composite Hydrogel: Synthesis, Characterization and Evaluation for the Removal of Methylene Blue from Aqueous Solutions. *Int. J. Biol. Macromol.* **2023**, *244*, 125251. [CrossRef]
299. Niu, Y.; Han, X.; Song, J.; Huang, L. Removal of Methylene Blue and Lead(II) via PVA/SA Double-Cross-Linked Network Gel Beads Loaded with Fe_3O_4 @KHA Nanoparticles. *New J. Chem.* **2021**, *45*, 5605–5620. [CrossRef]
300. Abutaleb, A.; Imran, M.; Zouli, N.; Khan, A.H.; Hussain, S.; Ali, M.A.; Bakather, O.; Gondal, M.A.; Khan, N.A.; Panchal, H.; et al. Fe_3O_4-Multiwalled Carbon Nanotubes-Bentonite as Adsorbent for Removal of Methylene Blue from Aqueous Solutions. *Chemosphere* **2023**, *316*, 137824. [CrossRef]
301. Chang, J.; Ma, J.; Ma, Q.; Zhang, D.; Qiao, N.; Hu, M.; Ma, H. Adsorption of Methylene Blue onto Fe_3O_4/Activated Montmorillonite Nanocomposite. *Appl. Clay Sci.* **2016**, *119*, 132–140. [CrossRef]
302. Barakat, M.A.; Kumar, R.; Halawani, R.F.; Al-Mur, B.A.; Seliem, M.K. Fe_3O_4 Nanoparticles Loaded Bentonite/Sawdust Interface for the Removal of Methylene Blue: Insights into Adsorption Performance and Mechanism via Experiments and Theoretical Calculations. *Water* **2022**, *14*, 3491. [CrossRef]
303. Maimaiti, T.; Hu, R.; Yuan, H.; Liang, C.; Liu, F.; Li, Q.; Lan, S.; Yu, B.; Yang, S.-T. Magnetic Fe_3O_4/TiO_2/Graphene Sponge for the Adsorption of Methylene Blue in Aqueous Solution. *Diam. Relat. Mater.* **2022**, *123*, 108811. [CrossRef]
304. Kazemi, J.; Javanbakht, V. Alginate Beads Impregnated with Magnetic Chitosan@Zeolite Nanocomposite for Cationic Methylene Blue Dye Removal from Aqueous Solution. *Int. J. Biol. Macromol.* **2020**, *154*, 1426–1437. [CrossRef]
305. Rahmi; Ishmaturrahmi; Mustafa, I. Methylene Blue Removal from Water Using H_2SO_4 Crosslinked Magnetic Chitosan Nanocomposite Beads. *Microchem. J.* **2019**, *144*, 397–402. [CrossRef]
306. Faaizatunnisa, N.; Ediati, R.; Fansuri, H.; Juwono, H.; Suprapto, S.; Hidayat, A.R.P.; Zulfa, L.L. Facile Green Synthesis of Core–Shell Magnetic MOF Composites (Fe_3O_4@SiO_2@HKUST-1) for Enhanced Adsorption Capacity of Methylene Blue. *Nano Struct. Nano Objects* **2023**, *34*, 100968. [CrossRef]
307. Wo, R.; Li, Q.-L.; Zhu, C.; Zhang, Y.; Qiao, G.; Lei, K.; Du, P.; Jiang, W. Preparation and Characterization of Functionalized Metal–Organic Frameworks with Core/Shell Magnetic Particles (Fe_3O_4@SiO_2@MOFs) for Removal of Congo Red and Methylene Blue from Water Solution. *J. Chem. Eng. Data* **2019**, *64*, 2455–2463. [CrossRef]
308. Aslam, S.; Zeng, J.; Subhan, F.; Li, M.; Lyu, F.; Li, Y.; Yan, Z. In Situ One-Step Synthesis of Fe_3O_4@MIL-100(Fe) Core-Shells for Adsorption of Methylene Blue from Water. *J. Colloid Interface Sci.* **2017**, *505*, 186–195. [CrossRef]
309. Mahmoodi, N.M.; Abdi, J.; Oveisi, M.; Alinia Asli, M.; Vossoughi, M. Metal-Organic Framework (MIL-100(Fe)): Synthesis, Detailed Photocatalytic Dye Degradation Ability in Colored Textile Wastewater and Recycling. *Mater. Res. Bull.* **2018**, *100*, 357–366. [CrossRef]
310. Wang, R.; Ge, C.; Xing, T.; Zhang, Y.; Zhang, Y.; Zhang, X. Facile Synthesis of Magnetic Hybrid Metal–Organic Frameworks with High Adsorption Capacity for Methylene Blue. *Appl. Organomet. Chem.* **2017**, *31*, e3798. [CrossRef]
311. Xu, Y.; Jin, J.; Li, X.; Song, C.; Meng, H.; Zhang, X. Adsorption Behavior of Methylene Blue on Fe_3O_4-Embedded Hybrid Magnetic Metal–Organic Framework. *Desalination Water Treat.* **2016**, *57*, 25216–25225. [CrossRef]
312. Li, L.; Liu, X.L.; Gao, M.; Hong, W.; Liu, G.Z.; Fan, L.; Hu, B.; Xia, Q.H.; Liu, L.; Song, G.W.; et al. The Adsorption on Magnetic Hybrid Fe_3O_4/HKUST-1/GO of Methylene Blue from Water Solution. *J. Mater. Chem. A* **2014**, *2*, 1795–1801. [CrossRef]
313. Shao, Y.; Zhou, L.; Bao, C.; Ma, J.; Liu, M.; Wang, F. Magnetic Responsive Metal–Organic Frameworks Nanosphere with Core–Shell Structure for Highly Efficient Removal of Methylene Blue. *Chem. Eng. J.* **2016**, *283*, 1127–1136. [CrossRef]
314. Rosa, E.V.; Fascineli, M.L.; da Silva, I.C.R.; Rodrigues, M.O.; Chaker, J.A.; Grisolia, C.K.; Moya, S.E.; Campos, A.F.C.; Sousa, M.H. Carbon Nitride Nanosheets Magnetically Decorated with Fe_3O_4 Nanoparticles by Homogeneous Precipitation: Adsorption-Photocatalytic Performance and Acute Toxicity Assessment. *Environ. Nanotechnol. Monit. Manag.* **2021**, *16*, 100549. [CrossRef]
315. Soni, S.; Bajpai, P.K.; Mittal, J.; Arora, C. Utilisation of Cobalt Doped Iron Based MOF for Enhanced Removal and Recovery of Methylene Blue Dye from Waste Water. *J. Mol. Liq.* **2020**, *314*, 113642. [CrossRef]
316. Ali, H.; Ismail, A.M. Fabrication of Magnetic Fe_3O_4/Polypyrrole/Carbon Black Nanocomposite for Effective Uptake of Congo Red and Methylene Blue Dye: Adsorption Investigation and Mechanism. *J. Polym. Environ.* **2023**, *31*, 976–998. [CrossRef]
317. ZabihiSahebi, A.; Koushkbaghi, S.; Pishnamazi, M.; Askari, A.; Khosravi, R.; Irani, M. Synthesis of Cellulose Acetate/Chitosan/SWCNT/Fe_3O_4/TiO_2 Composite Nanofibers for the Removal of Cr(VI), As(V), Methylene Blue and Congo Red from Aqueous Solutions. *Int. J. Biol. Macromol.* **2019**, *140*, 1296–1304. [CrossRef] [PubMed]
318. Lei, C.; Wen, F.; Chen, J.; Chen, W.; Huang, Y.; Wang, B. Mussel-Inspired Synthesis of Magnetic Carboxymethyl Chitosan Aerogel for Removal Cationic and Anionic Dyes from Aqueous Solution. *Polymer* **2021**, *213*, 123316. [CrossRef]
319. Munagapati, V.S.; Wen, H.-Y.; Gollakota, A.R.K.; Wen, J.-C.; Lin, K.-Y.A.; Shu, C.-M.; Yarramuthi, V.; Basivi, P.K.; Reddy, G.M.; Zyryanov, G.V. Magnetic Fe_3O_4 Nanoparticles Loaded Guava Leaves Powder Impregnated into Calcium Alginate Hydrogel Beads (Fe_3O_4-GLP@CAB) for Efficient Removal of Methylene Blue Dye from Aqueous Environment: Synthesis, Characterization, and Its Adsorption Performance. *Int. J. Biol. Macromol.* **2023**, *246*, 125675. [CrossRef]

320. Zhao, W.; Zhao, Y.; Zhang, H.; Hao, C.; Zhao, P. Efficient Removal of Cationic and Anionic Dyes by Surfactant Modified Fe_3O_4 Nanoparticles. *Colloids Surf. A Physicochem. Eng. Asp.* **2022**, *633*, 127680. [CrossRef]
321. Bai, L.; Li, Z.; Zhang, Y.; Wang, T.; Lu, R.; Zhou, W.; Gao, H.; Zhang, S. Synthesis of Water-Dispersible Graphene-Modified Magnetic Polypyrrole Nanocomposite and Its Ability to Efficiently Adsorb Methylene Blue from Aqueous Solution. *Chem. Eng. J.* **2015**, *279*, 757–766. [CrossRef]
322. Gong, J.; Yao, K.; Liu, J.; Wen, X.; Chen, X.; Jiang, Z.; Mijowska, E.; Tang, T. Catalytic Conversion of Linear Low Density Polyethylene into Carbon Nanomaterials under the Combined Catalysis of Ni_2O_3 and Poly(Vinyl Chloride). *Chem. Eng. J.* **2013**, *215–216*, 339–347. [CrossRef]
323. Ai, L.; Zhang, C.; Chen, Z. Removal of Methylene Blue from Aqueous Solution by a Solvothermal-Synthesized Graphene/Magnetite Composite. *J. Hazard. Mater.* **2011**, *192*, 1515–1524. [CrossRef]
324. Zhang, P.; Xiang, M.; Liu, H.; Yang, C.; Deng, S. Novel Two-Dimensional Magnetic Titanium Carbide for Methylene Blue Removal over a Wide PH Range: Insight into Removal Performance and Mechanism. *ACS Appl. Mater. Interfaces* **2019**, *11*, 24027–24036. [CrossRef] [PubMed]
325. Tara, N.; Siddiqui, S.I.; Nirala, R.K.; Abdulla, N.K.; Chaudhry, S.A. Synthesis of Antibacterial, Antioxidant and Magnetic Nigella Sativa-Graphene Oxide Based Nanocomposite BC-GO@Fe_3O_4 for Water Treatment. *Colloid Interface Sci. Commun.* **2020**, *37*, 100281. [CrossRef]
326. Anushree, C.; Philip, J. Efficient Removal of Methylene Blue Dye Using Cellulose Capped Fe_3O_4 Nanofluids Prepared Using Oxidation-Precipitation Method. *Colloids Surf. A Physicochem. Eng. Asp.* **2019**, *567*, 193–204. [CrossRef]
327. Tran, H.V.; Bui, L.T.; Dinh, T.T.; Le, D.H.; Huynh, C.D.; Trinh, A.X. Graphene Oxide/Fe_3O_4/Chitosan Nanocomposite: A Recoverable and Recyclable Adsorbent for Organic Dyes Removal. Application to Methylene Blue. *Mater. Res. Express* **2017**, *4*, 035701. [CrossRef]
328. Wang, H.; Zhou, P.; Guo, R.; Wang, Y.; Zhan, H.; Yuan, Y. Synthesis of Rectorite/Fe3O4/ZnO Composites and Their Application for the Removal of Methylene Blue Dye. *Catalysts* **2018**, *8*, 107. [CrossRef]
329. Chishti, A.N.; Guo, F.; Aftab, A.; Ma, Z.; Liu, Y.; Chen, M.; Gautam, J.; Chen, C.; Ni, L.; Diao, G. Synthesis of Silver Doped Fe_3O_4/C Nanoparticles and Its Catalytic Activities for the Degradation and Reduction of Methylene Blue and 4-Nitrophenol. *Appl. Surf. Sci.* **2021**, *546*, 149070. [CrossRef]
330. Alinezhad, H.; Zabihi, M.; Kahfroushan, D. Design and Fabrication the Novel Polymeric Magnetic Boehmite Nanocomposite (Boehmite@ Fe_3O_4@PLA@SiO_2) for the Remarkable Competitive Adsorption of Methylene Blue and Mercury Ions. *J. Phys. Chem. Solids* **2020**, *144*, 109515. [CrossRef]
331. Saiphaneendra, B.; Saxena, T.; Singh, S.A.; Madras, G.; Srivastava, C. Synergistic Effect of Co-Existence of Hematite (α-Fe_2O_3) and Magnetite (Fe_3O_4) Nanoparticles on Graphene Sheet for Dye Adsorption. *J. Environ. Chem. Eng.* **2017**, *5*, 26–37. [CrossRef]
332. Chen, J.; Chen, H. Removal of Anionic Dyes from an Aqueous Solution by a Magnetic Cationic Adsorbent Modified with DMDAAC. *New J. Chem.* **2018**, *42*, 7262–7271. [CrossRef]
333. de Araújo Padilha, C.E.; da Costa Nogueira, C.; de Santana Souza, D.F.; de Oliveira, J.A.; dos Santos, E.S. Organosolv Lignin/Fe_3O_4 Nanoparticles Applied as a β-Glucosidase Immobilization Support and Adsorbent for Textile Dye Removal. *Ind. Crops Prod.* **2020**, *146*, 112167. [CrossRef]
334. Yao, L.; Yang, J.; Zhang, P.; Deng, L. In Situ Surface Decoration of Fe_3C/Fe_3O_4/C Nanosheets: Towards Bi-Functional Activated Carbons with Supercapacitance and Efficient Dye Adsorption. *Bioresour. Technol.* **2018**, *256*, 208–215. [CrossRef]
335. Zhang, C.; Dai, Y.; Wu, Y.; Lu, G.; Cao, Z.; Cheng, J.; Wang, K.; Yang, H.; Xia, Y.; Wen, X.; et al. Facile Preparation of Polyacrylamide/Chitosan/Fe_3O_4 Composite Hydrogels for Effective Removal of Methylene Blue from Aqueous Solution. *Carbohydr. Polym.* **2020**, *234*, 115882. [CrossRef]
336. Subhan, F.; Aslam, S.; Yan, Z.; Khan, M.; Etim, U.J.; Naeem, M. Effective Adsorptive Performance of Fe_3O_4@SiO_2 Core Shell Spheres for Methylene Blue: Kinetics, Isotherm and Mechanism. *J. Porous Mater.* **2019**, *26*, 1465–1474. [CrossRef]
337. Lei, Y.; Zhang, X.; Meng, X.; Wang, Z. The Preparation of Core–Shell Fe_3O_4@SiO_2 Magnetic Nanoparticles with Different Surface Carboxyl Densities and Their Application in the Removal of Methylene Blue. *Inorg. Chem. Commun.* **2022**, *139*, 109381. [CrossRef]
338. Qi, L.; Jiaqi, Z.; Yimin, D.; Danyang, L.; Shengyun, W.; Ling, C. Facile Synthesis of 5-Aminoisophthalic Acid Functionalized Magnetic Nanoparticle for the Removal of Methylene Blue. *J. Mater. Sci. Mater. Electron.* **2020**, *31*, 457–468. [CrossRef]
339. Jiaqi, Z.; Yimin, D.; Danyang, L.; Shengyun, W.; Liling, Z.; Yi, Z. Synthesis of Carboxyl-Functionalized Magnetic Nanoparticle for the Removal of Methylene Blue. *Colloids Surf. A Physicochem. Eng. Asp.* **2019**, *572*, 58–66. [CrossRef]
340. Tan, X.; Lu, L.; Wang, L.; Zhang, J. Facile Synthesis of Bimodal Mesoporous Fe_3O_4@SiO_2 Composite for Efficient Removal of Methylene Blue. *Eur. J. Inorg. Chem.* **2015**, *2015*, 2928–2933. [CrossRef]
341. Zheng, J.; Cheng, C.; Fang, W.-J.; Chen, C.; Yan, R.-W.; Huai, H.-X.; Wang, C.-C. Surfactant-Free Synthesis of a Fe_3O_4@ZIF-8 Core–Shell Heterostructure for Adsorption of Methylene Blue. *CrystEngComm* **2014**, *16*, 3960–3964. [CrossRef]
342. Kraithep, C.; Sajomsang, W.; Minami, H.; Busabok, C.; Tangboriboonrat, P.; Chaiyasat, P.; Chaiyasat, A. Fabrication of Porous Polymer Particles Containing $BiVO_4$ and Fe_3O_4 Nanoparticles Using Block Copolymer as Porogen for Effective Dye Removal. *Surf. Interfaces* **2023**, *37*, 102738. [CrossRef]
343. Srisawang, N.; Chaiyasat, A.; Ngernchuklin, P.; Chaiyasat, P. Novel Reusable PH-Responsive Photocatalyst Polymeric Microcapsules for Dye Treatment. *Int. J. Energy Res.* **2021**, *45*, 7535–7548. [CrossRef]

344. Benhalima, T.; Ferfera-Harrar, H.; Saha, N.; Saha, P. Fe_3O_4 Imbuing Carboxymethyl Cellulose/Dextran Sulfate Nanocomposite Hydrogel Beads: An Effective Adsorbent for Methylene Blue Dye Pollutant. *J. Macromol. Sci. Part A* **2023**, *60*, 442–461. [CrossRef]
345. Yusuf, M.S.; Rahmasari, R. Synthesis Processing Condition Optimization of Citrate Stabilized Superparamagnetic Iron Oxide Nanoparticles Using Direct Co-Precipitation Method. *Biomed. Pharmacol. J.* **2021**, *14*, 1533–1542. [CrossRef]
346. Verma, M.; Dwivedi, P.K.; Saxena, N.S. Hollow Silica Nanoparticles Synthesized from Core-Shell Nanoparticles as Highly Efficient Adsorbent for Methylene Blue and Its Invitro Release: Mechanism and Kinetics Study. *Colloids Surf. A Physicochem. Eng. Asp.* **2020**, *587*, 124333. [CrossRef]
347. Bruschi, M.L. Mathematical Models of Drug Release. In *Strategies to Modify the Drug Release from Pharmaceutical Systems*; Elsevier: Amsterdam, The Netherlands, 2015; pp. 63–86, ISBN 978-0-08-100092-2.
348. Ribeiro, S.C.; de Lima, H.H.C.; Kupfer, V.L.; da Silva, C.T.P.; Veregue, F.R.; Radovanovic, E.; Guilherme, M.R.; Rinaldi, A.W. Synthesis of a Superabsorbent Hybrid Hydrogel with Excellent Mechanical Properties: Water Transport and Methylene Blue Absorption Profiles. *J. Mol. Liq.* **2019**, *294*, 111553. [CrossRef]
349. Wang, W.; Zhang, W.; Sun, H.; Li, X.; Du, Q.; Wei, C.; Ge, X.; Li, C. The Transition from Locally Excited States to Twisted Intramolecular Charge Transfer States for Fluorescence Methylene Blue Labeled in Biodegradable Silica Particles. *J. Mol. Liq.* **2019**, *291*, 111312. [CrossRef]
350. Peppas, N.A.; Sahlin, J.J. A Simple Equation for the Description of Solute Release. III. Coupling of Diffusion and Relaxation. *Int. J. Pharm.* **1989**, *57*, 169–172. [CrossRef]
351. Korsmeyer, R.W.; Gurny, R.; Doelker, E.; Buri, P.; Peppas, N.A. Mechanisms of Solute Release from Porous Hydrophilic Polymers. *Int. J. Pharm.* **1983**, *15*, 25–35. [CrossRef]
352. Chahal, C.; van den Akker, B.; Young, F.; Franco, C.; Blackbeard, J.; Monis, P. Pathogen and Particle Associations in Wastewater. *Adv. Appl. Microbiol.* **2016**, *97*, 63–119. [CrossRef]
353. Balouiri, M.; Sadiki, M.; Ibnsouda, S.K. Methods for in Vitro Evaluating Antimicrobial Activity: A Review. *J. Pharm. Anal.* **2016**, *6*, 71–79. [CrossRef]